Stoichiometry driven tuning of physical properties in epitaxial Fe_3 − xCr_xO_4 thin films

Pâmella Vasconcelos Borges Pinho, Alain Chartier, Denis Menut, Antoine Barbier, Myrtille O.J.Y. Hunault, Philippe Ohresser, Cécile Marcelot, Bénédicte Warot-Fonrose, Frédéric Miserque, Jean-Baptiste Moussy

Stoichiometry Driven Tuning of Physical Properties in Spinel Oxide Layers

Pâmella Vasconcelos Borges Pinho[a,b]*, Alain Chartier[a], Denis Menut[c], Antoine Barbier[b], Myrtille O.J.Y. Hunault[c], Philippe Ohresser[c], Cécile Marcelot[d], Bénédicte Warot-Fonrose[d], Frédéric Miserque[a], Jean-Baptiste Moussy[b]*

[a] *Université Paris-Saclay, CEA, Service de la Corrosion et du Comportement des Matériaux dans leur Environnement, 91191, Gif-sur-Yvette, France ;* [b] *Université Paris-Saclay, CEA, CNRS, SPEC, 91191, Gif-sur-Yvette, France ;* [c] *Synchrotron SOLEIL, L'Orme des Merisiers, Saint Aubin BP 48, 91192 Gif-sur-Yvette, France ;* [d] *CEMES-CNRS, Université de Toulouse, CNRS, 29 rue Jeanne Marvig, 31055 Toulouse, France*

* E-mail: pamella.vasconcelos@esrf.fr; jean-baptiste.moussy@cea.fr

Abstract

Tuning magnetic and electronic transport properties in spinel oxides requires a faithful description between chemical composition and cation site-occupation. Here this challenge is addressed using $Fe_{3-x}Cr_xO_4$ thin films grown by oxygen-assisted molecular-beam epitaxy within a wide range of composition ($0.0 \leq x \leq 1.2$). Spectroscopic measurements (*e.g.*, X-ray magnetic circular dichroism), refined by theoretical simulations (*e.g.*, crystal field multiplet), are performed to establish a quantitative link between chromium content, Fe^{2+}/Fe^{3+} site-occupation and macroscopic physical properties of the layers. It is found that $Fe_{3-x}Cr_xO_4$ thin films (*i*) delay the transition from inverse to normal spinel configuration with increasing chromium content and (*ii*) promote collinear spin structure, at odds with bulk material. As a result, strong antiferromagnetic interactions are preserved between spins in tetrahedral and octahedral spinel sublattices, so that chromium-rich thin films exhibit Curie temperatures above room temperature and higher magnetization. Electron hopping is also favored by this singular cation distribution and electronic band gap is smaller than expected for these thin films. The cation site-occupation is therefore a key feature to consider for applications of $Fe_{3-x}Cr_xO_4$ thin films in spintronics and photocatalysis, as it enables manipulation of magnetic properties (Curie temperature and magnetization) and band gap engineering.

Keywords: epitaxial thin films, iron-chromium spinel oxides, cation site-occupation, electronic conductivity, magnetism

1. Introduction

In the search for novel materials, oxides with spinel structure are very attractive due to their unique physicochemical properties. In these oxides, multivalence cations laid out on a geometrically frustrated network of octahedral sites and a diamond lattice formed by tetrahedral sites, termed here Oh-sites and Td-sites respectively. The complexity of the spinel structure opens the way for tailoring the functional properties of these materials by incorporating different metal cations into the host matrix [1]. Magnetite (Fe_3O_4) is for example a well-known half-metallic ferrite (conduction electrons 100% spin polarized) with high Curie temperature (T_C = 850 K), which has often been envisioned for use in future high-performance spintronic devices, such as magnetic memories and spin field-effect transistors [2–4]. By partially replacing the iron in the magnetite structure, other physical properties and thus novel (or improved) applications can be found. Insulating spinel ferrites (*i.e.*, $NiFe_2O_4$, $MnFe_2O_4$ or $CoFe_2O_4$) have been studied for their spin filtering abilities [5,6], while MgAl- and NiZnAl-ferrites have been reported recently for their good spin dynamics properties [7,8]. In other research fields, such as catalysis, iron-chromium spinels ($Fe_{3-x}Cr_xO_4$) shows promising application in the decomposition of organic pollutants in wastewaters using H_2O_2 in a heterogeneous Fenton system [9,10]. It has been shown that adding small concentration of Cr leads to significant increase on the catalyst activity in the oxidation process of dyes, exhibiting complete discoloration and high degree of mineralization. $Fe_{3-x}Cr_xO_4$ are also relevant oxides in corrosion science [11,12], since they appear frequently on the surface of metallic materials (*e.g.*, Fe-Cr based alloys) during the oxidation process. This oxide layer plays a major role in the material durability as it governs the electronic and cationic transport between the alloy and the oxidizing medium.

As the spinel structure is able to accommodate much cation disorder, new functionalities are available that will depend mainly on the local structure of the substituents, *i.e.*, valences, distribution among the cation sublattices (tetrahedral or octahedral) and relative strength of competing effects. In this regard, the iron-chromium spinels ($Fe_{3-x}Cr_xO_4$, where x is the Cr content) are of considerable interest. This series forms a complete solid solution intrinsically defect free for the $0 \leq x \leq 2$ range, in which the two limiting compositions have highly distinct functional properties. $FeCr_2O_4$ presents a normal spinel structure with Fe^{2+} cations in tetrahedral sites (Td-sites) and Cr^{3+} cations in octahedral sites (Oh-sites). In contrast to Fe_3O_4, which has an inverse spinel structure (Fe^{3+} in Td-sites and both Fe^{2+} and Fe^{3+} randomly distributed in Oh-sites), $FeCr_2O_4$ has a conical spiral spin structure [13], low Curie temperature (T_C = 80 K) and an insulator behavior [14].

The cation distribution for intermediate compositions can be written as $(Fe^{3+}_yFe^{2+}_{1-y})[Fe^{2+}_yFe^{3+}_{2-x-y}Cr^{3+}_x]O_4$, where () and [] represent Td-sites and Oh-sites, respectively, and the inversion parameter (y) accounts for cation disorder. Note that in this general formula Cr is expected

to have the stable valence of 3+ and occupies exclusively Oh-sites, while Fe^{2+} and Fe^{3+} ions are distributed between Td and Oh-sites. According to Mössbauer spectroscopy and magnetic measurements performed on polycrystalline samples [15,16], three regions are observed in the cation distribution diagram of $Fe_{3-x}Cr_xO_4$ depending on Cr content: (I) $x < 0.5$, (II) $0.6 < x < 1.2$ and (III) $x > 1.3$. In region I, the spinel structure assumes a rather inverse configuration (mainly Fe^{3+} at Td-sites) with y closes to 1. In region II, an intermediate configuration (Fe^{2+} and Fe^{3+} at Td and Oh-sites) is observed, where y gradually decreases from 0.7 to 0. In region III, these compounds keep a complete normal configuration ($y = 0$, only Fe^{2+} at Td-sites). The presence of Fe^{2+} ions in Td-sites introduces phase transitions upon cooling (*e.g.*, cubic-to-tetragonal and tetragonal-to-orthorhombic), which are usually followed by a magnetic order. This magnetic ordering is stabilized by reducing the lattice symmetry through a spin-lattice coupling (cooperative Jahn-Teller effect) and it is frequently assimilated to the origin of lower moments in Cr-containing spinels. The detailed of these complex magnetic and structural phase transitions are however still under debate [13,17,18].

Cation disorder also plays an important role in the conduction mechanisms of the $Fe_{3-x}Cr_xO_4$ series as it impacts the easy electron transfer between Fe^{2+}-Fe^{3+} in octahedral sites, which is the well-known reason for the very high conductivity of magnetite [19]. The substitution of Fe cations for Cr in magnetite converts the half-metal host ferrimagnet into either a semiconductor or an insulator, depending on the Cr content [20,21]. As semiconductors, $Fe_{3-x}Cr_xO_4$ thin films can be of considerable interest for photocatalysis, particularly for the compositions whose band gap remains small, enabling visible light harvesting [14,20]. Although it is possible to control the band gap of $Fe_{3-x}Cr_xO_4$ by changing the Cr content, the electronic and optical properties of this solid solution have received relatively little attention.

Despite the many applications of the $Fe_{3-x}Cr_xO_4$ series, most previous works [13,15] are based on bulk-like samples, while thin films have received limited consideration [20,22,23]. Numerous studies have shown that physical and chemical properties of thin films strongly deviate from the bulk, depending on the growth method [24], film thickness [25], and surface and interface effects [26]. Since the growth of functional optical and magnetic thin films is a key technology for modern applications in photocatalysis or spintronic devices, we propose here a comprehensive study on the effect of substitutional Cr on the physical and chemical properties of epitaxial $Fe_{3-x}Cr_xO_4$ thin films. The aim is to dissociate the compositional effect (including cation disorder) from other types of defects in order to better comprehend intrinsic properties of these materials, such as their magnetic and conduction behavior. For this purpose, we have followed a thorough strategy described in detail below, in which (*i*) experimental measurements are systematically enriched with modeling/simulations to improve their relevance and (*ii*) microscopic-scale data are acquired to feed models that help unravel macroscopic properties. On this basis, we show that thin films delay the

transition from the inverse spinel (Fe_3O_4) to the normal one ($FeCr_2O_4$) – *i.e.*, there are Fe^{2+}/Fe^{3+} ions sitting at both Td and Oh-sites even in chromium-rich spinels – and promote collinear spin structure, at odds with bulk material. The difference in both cation site occupancy and spin order results in different magnetic and conduction behavior of the $Fe_{3-x}Cr_xO_4$ thin films compared to bulk. We demonstrate that the presence of Fe^{3+}/Fe^{2+} ions in Td and Oh-sites yields a strong antiferromagnetic interaction between these sites, resulting in Curie temperatures above room temperature for chromium-rich spinels. Additionally, we evidence that the electronic conductivity of the series is described by small polaron model based on Fe^{2+}/Fe^{3+} concentration in Oh-sites and the possibility of this pair to form a continuous conductive pathway (uninterrupted by Cr^{3+} cations). Hence, a quantitative link is established between composition – cationic occupation – magnetic properties – and electronic transport in iron-chromium spinels.

Besides growing and characterizing functional optical and magnetic semiconductors, experimental data collected here can be used as a database to study the complex corrosion layers formed by nanoscale, poorly crystallized films of variable $Fe_{3-x}Cr_xO_4$ composition. They are important inputs to microscopic and mesoscopic models applied to corrosion, such as the diffusion Poisson coupled model [27], for which solid-state transport of charge carriers (point defects, ions, electrons or holes) in the oxide layer is considered, so the physical mechanism for transport has to be known (which is not always the case, especially for intermediate $Fe_{3-x}Cr_xO_4$ compositions).

2. Material and methods

2.1. Thin film growth

To produce $Fe_{3-x}Cr_xO_4$ thin films ($0 \leq x \leq 1.7$) with a well-defined composition and single crystalline structure, we employed the oxygen-plasma-assisted molecular beam epitaxy (O-MBE) technique. We chose this method because it enables the synthesis of this series with a perfect control of the chromium content (x) by using individual Knudsen effusion cells under a reactive atomic oxygen plasma. The growth was followed in real time using a reflection high-energy electron diffraction (RHEED) gun, which allowed us to control the crystalline structure of the atomic layers. The metal evaporation rate was calibrated *in situ* using a quartz balance. The evaporation rate of Fe was fixed to 0.35 Å·min^{-1}, while the one of Cr varied from 0.1 to 0.5 Å·min^{-1} in order to adjust the composition. The thickness of the films was about 15 to 20 nm with average roughness of 0.7 nm, as confirmed *ex situ* by X-ray reflectivity (XRR) measurements. See supporting information and the literature [5,28] for more details on these experimental techniques.

2.2. Thin film characterization

Following growth, we used several characterization techniques to obtain chemical (composition and redox) and structural (phase and dimensions) information from the thin films. The stoichiometry of the $Fe_{3-x}Cr_xO_4$ films were verified *ex situ* by X-ray photoemission spectroscopy (XPS) measurements using an *Escalab 250 XI* spectrometer with a monochromatic Al Kα source ($h\nu$ = 1486.6 eV). High-resolution XPS spectra were acquired using 5 eV pass energy. There was no need for charge compensation. The crystalline phase and quality of the films were determined by X-ray diffraction (XRD) using a standard diffractometer (*Bruker D8 Advance*) running in the Bragg–Brentano geometry and rocking curve. For selected samples, high-resolution XRD (HRXRD) were performed on MARS beam line [29] of SOLEIL synchrotron.

The film microstructure was investigated via high-resolution transmission electron microscopy (HRTEM) on CEMES-CNRS laboratory. The micrographs were recorded using an *I2TEM microscope* operating at 300 kV and fitted with an objective lens aberration corrector (point resolution of 80 pm). Cross-sectional samples were prepared by cutting along the $[1\bar{1}00]$ and/or $[\bar{1}2\bar{1}0]$ crystallographic directions before thinning by mechanical grinding and ion milling (using a precision ionic polish system) in order to achieve electron transparency. Complementary quantitative elemental analyses were performed by electron energy loss spectroscopy (EELS) and energy-dispersive X-ray spectroscopy (EDX), respectively integrated at the *I2TEM* and *CM20FEG microscope* (200 kV).

X-ray absorption near-edge structure (XANES) and extended X-ray absorption fine structure (EXAFS) measurements were carried out on MARS Beamline [30] of synchrotron SOLEIL. Spectra were recorded at the K-edge of Cr (5989 eV) and Fe (7112 eV) in total fluorescence yield (TFY) mode, which enables to probe the entire film. Both XANES and EXAFS data presented here is an average of four spectra obtained successively. The oxidation state and electronic structure of the absorbing elements at the XANES region was investigated using fingerprint analysis within the ATHENA software [31]. The first cation-neighbors bond distances and the structural disorder around the cations were obtained by treating EXAFS data within ARTEMIS software [31]. See Supporting Information for more details on the data treatment.

After describing structural and chemical properties of the $Fe_{3-x}Cr_xO_4(111)$ thin films, physical measurements were performed. In-plane magnetic measurements were carried out using a VSM magnetometer in a quantum design physical properties measurement system (*7 Tesla PPMS-VSM*). Magnetic hysteresis loops were recorded at 300 K with magnetic field up to 2 Tesla. The field was applied along the $[11\bar{2}0]$ axis of the α-$Al_2O_3(0001)$ substrate. In order to obtain a signal from the magnetic deposited layers only, the diamagnetic contributions of the sample holder and substrate

were removed by subtracting linear contributions (whose slope is about 10^{-2} kA m^{-1} T^{-1}) from raw data. The *PPMS* system was also used to perform in-plane electrical measurements using standard four-probe dc method. Resistance curves were recorded as function of temperature (T: 60 → 300 K) with no applied field. Resistivity (ρ) was then calculated by dividing the resistance obtained from the measurement data by the distance between probes and multiplying by the iron chromite layer volume.

The Cr and Fe cation site distribution was determined by exploring the $L_{2,3}$-edge X-ray absorption (XAS) and circular dichroism (XMCD) measurements performed on DEIMOS Beamline [32,33] of synchrotron SOLEIL. The samples were saturated with a magnetic induction of ±2.0 T parallel to the wave vector of the incident photons. Spectra were acquired at room temperature with an angle of 60° between the beam and the sample surface. The absorption signal was recorded in total electron yield (TEY) mode. The photocurrent of the electrons flowing from the sample was measured with electrometers connected to a counting card. Because electrons are emitted mostly from the first 2–5 nm of a sample, this approach is very sensitive to the surface. All measurements were performed in UHV conditions, *i.e.,* base pressure inside the chamber of about 10^{-10} mbar.

2.3. Crystal field multiplet calculations

XAS and XMCD spectra were interpreted using crystal field multiplet (CFM) calculations performed on the quantum many-body script code QUANTY [34–36] within the graphical interface CRISPY [37]. Independent contributions for the Cr (Cr^{3+}_{Oh}) and Fe (Fe^{2+}_{Td}, Fe^{2+}_{Oh}, Fe^{3+}_{Td} and Fe^{3+}_{Oh}) sites were considered for the simulations. The atomic parameters for each cation site were optimized in this work (see Supporting Information for details) and are in good agreement with the literature [38–40]. For all simulated spectra, the ground state was populated according to a Boltzmann distribution at 300 K. The XAS spectra were calculated by solving Green's functions in second quantization. The resulting sharp peaks were convoluted with a Lorentzian function (FWHM = 0.2 eV for L_3 edge and 0.6 eV for L_2 edge) and a Gaussian function (FWHM = 0.5 eV) to mimic the experimental broadening of the spectral lines. The weighting factors for each Fe contribution to the XMCD spectrum were fitted to give the best agreement with experiment.

2.4. Atomistic spin dynamics

Curie temperatures of $Fe_{3-x}Cr_xO_4$ with different cationic arrangements were simulated using an atomistic spin model (ASM) with the VAMPIRE software package [41]. Details of this model is given in Supporting Information. The simulated system consisted of a rigid cube ($8.4 \times 8.4 \times 8.4$ nm^3 in size), for which periodic boundary conditions (PBC) were applied to reduce finite-size effects by eliminating the surface. Herein, the lattice parameter and the inversion ratio used as input for the

simulation were the ones presented in the literature [15]. The cations were randomly distributed among the Td and Oh sublattices. The temperature-dependent magnetization curves were calculated via the Monte Carlo algorithm, using 10,000 equilibration steps and 10,000 averaging steps. A good estimate of the T_C was usually obtained within 1% of the experimental values.

3. Results and discussion

3.1. Epitaxial growth and structural characterization

Stoichiometric series of epitaxial $Fe_{3-x}Cr_xO_4(111)$ thin films were grown on single crystalline α-$Al_2O_3(0001)$ substrates by O-MBE, as sketched in **Figure 1a**. Several characterization techniques were employed in order to confirm the high purity and single-crystalline nature of our films. First, we followed in real time the crystalline structure of the oxide formed during deposition using reflection high-energy electron diffraction (RHEED). As shown in **Figure 1b** insets, in comparison with the RHEED patterns along the $[\bar{1}2\bar{1}0]$ direction of the corundum substrate (bottom inset), the oxide layer exhibit additional (½,½)-type rods (green arrows) typical of the spinel structure [5]. For $x \leq 1.4$, RHEED patterns (**Figure S1**, Supporting Information) have sharp diffraction streaks and no spots, which are representative of bidimensional growth mode without secondary phases. Likewise, θ-2θ X-ray diffraction (XRD) patterns exhibit only (*hhh*) peaks corresponding to the (111) orientation of the spinel structure (**Figure S2**), indicating the textured single-phase quality of these films. **Figure 1c** shows a close-up view of the (222) peak where the appearance of Laue oscillations reflects the structural homogeneity of the film and low density of defects. For $x \leq 1.4$, the Bragg peaks are striking and the rocking curve obtained on the (222) peak ($\Delta\Omega = 0.2°$) is characteristic of high crystallinity. Meanwhile, for $x > 1.4$, the Bragg peaks are broader and the Laue oscillations are indistinct due to decrease of the crystalline quality. These compounds are thus excluded from further analysis.

The layer-substrate interface and structural defects were also evaluated by cross-sectional transmission electron microscopy (TEM) images. **Figure 1b** depicts TEM images of a representative $Fe_{2.8}Cr_{0.2}O_4$ film studied along the $[\bar{1}2\bar{1}0]$ direction. Low magnification TEM image (**Figure 1b$_1$**) shows that the film is homogeneous and has a constant thickness of about 15 nm. These results are consistent with the low roughness deduced from atomic force micrographs (**Figure S3**) and the thickness obtained from the fit of X-ray reflectivity (**Figure S4**) patterns and the fit of Laue oscillations (**Figure S5**). High-resolution TEM (HRTEM) micrographs (**Figure 1b$_2$**) show the (111) spinel planes oriented parallel to the substrate surface. We notice perfectly flat and abrupt $Fe_{2.8}Cr_{0.2}O_4/Al_2O_3$ interface with no noticeable parasite phases at atomic scale. Antiphase boundaries (APBs) associated with nucleation of islands on early stages of the film growth are also observed.

This stacking defect results in half-lattice translation of the cationic sublattice and influences greatly the electrical transport and magnetic properties of thin films. This phenomenon has been widely studied in epitaxial Fe_3O_4 [25,42] and it will be discussed for $Fe_{3-x}Cr_xO_4$ later. This HRTEM image is representative of all samples herein presented and confirms the epitaxial structure of our thin films.

For this iron-chromium spinel system, the in-plane lattice mismatch is about 8% and the spinel structure is quickly relaxed. A series of spaced contrasts appears on the substrate/film interface of the HRTEM micrographs, which may be attributed to misfit dislocations that takes part on the relaxation mechanism of these films. A slightly compressive strain however persists. As shown in **Figure 1d**, the out-of-plane lattice parameter (*c*) – extracted from the fit of the (222) Bragg peaks with a Gaussian function – are found to be slightly smaller than expected. For instance, the lattice parameter of $Fe_{2.8}Cr_{0.2}O_4$ film grown on Al_2O_3(0001) is 0.835 ± 0.001 nm while the bulk value is 0.8394 ± 0.0001 nm [43]. X-ray absorption fine structure (EXAFS) at Fe K-edge and HRTEM micrographs corroborate with these results. Analysis of the average nearest-neighbor Fe–O, Fe–M_{Oh} and Fe–Fe_{Td} bond distances reveals that the fitted distances lie below those for bulk $Fe_{3-x}Cr_xO_4$ (**Figure S6**, see Supporting Information for more details). In addition, the deduced interplanar distances (**Figure 1b2**) of 0.48 nm for planes parallel to the interface and 0.28 nm for planes perpendicular to the interface are also slightly smaller from the (111) and (220) interplanar spacing obtained for bulk samples (*i.e.*, 0.49 nm and 0.30 nm, respectively). These values remained constant across the entire profile of the $Fe_{2.8}Cr_{0.2}O_4$ film and confirms the small shrinkage of the spinel lattice.

The first evidence of the influence of Cr content was observed in the unit cell parameter (*c*), which exhibits a non-linear variation with composition (*x*). As shown in **Figure 1d**, apparently the behavior of the system can be divided into three distinct regions: (I) $0 < x < 0.5$, (II) $0.6 < x < 1.3$ and (III) $1.4 < x < 2.0$. In summary, the cell parameter decreases for *x* up to 0.5, increases for values between 0.6 and 1.3 and then decreases again for *x* greater than 1.4. This same behavior has been stated in the literature for bulk-like samples [15,43] and it is typically associated to changes in the cation distribution among tetrahedral and octahedral sublattices. The small reductions of *c* parameter for $x < 0.5$ results from the replacement of Fe^{3+} by slightly smaller Cr^{3+} in Oh-sites, whereas the enhancement of *c* parameters for $0.6 < x < 1.3$ can be understood by the displacement of larger Fe^{2+} into Td-sites. Indeed, orbitally active Fe^{2+} cations in Td-sites lead to tetragonal distortions due to cooperative Jahn-Teller effects [13]. For compositions with *x* over 1.4, films are assumed to have the normal type of spinel structure, so the *c* parameter decreases again because Fe^{3+} cations are replaced by smaller Cr^{3+} in Oh-sites. Understanding the mechanism that prompts Fe^{2+} to migrate from Oh to Td-sites can be very interesting. In order to account for changes in the local environment of the cations, chemical analyses were performed as detailed in the next sections.

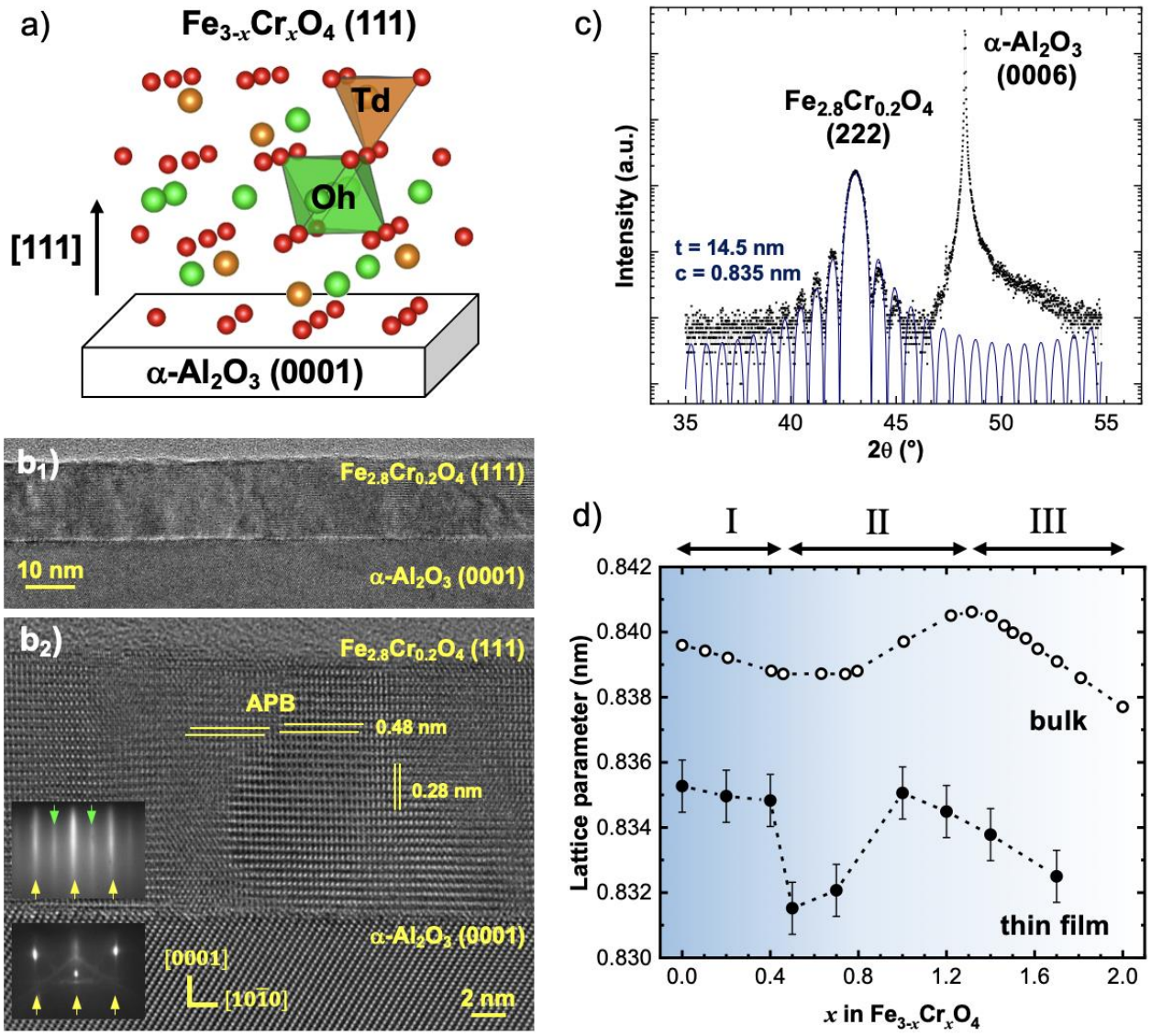

Figure 1. Structural characterization of $Fe_{3-x}Cr_xO_4$ thin films. (a) Schematic representation of $Fe_{3-x}Cr_xO_4$ epitaxial thin films grown on sapphire, highlighting Oh-sites (green) and Td-sites (orange). (b) Cross-sectional TEM images of $Fe_{2.8}Cr_{0.2}O_4$ films recorded along the $[\bar{1}2\bar{1}0]$ direction. Low magnification TEM (b_1) shows the homogeneity in thickness and structure of the 14.5 nm thick film. HRTEM image (b_2) depicts the deduced interplanar distances for this film, highlighting an APB. In inset, the corresponding RHEED patterns of the $Fe_{3-x}Cr_xO_4$ (top) assigned in the hexagonal real space of the substrate (bottom). (c) θ–2θ XRD scan of the (222) Bragg peak for $Fe_{2.8}Cr_{0.2}O_4$. The intense peak at ~48° corresponds to the (0006) Bragg peak of the sapphire substrate. (d) Room temperature out-of-plane lattice cell parameters (*c*) of compositions $Fe_{3-x}Cr_xO_4$ for reference bulk samples [43] (white circles) and thin films (black circles). Dashed lines are a guide to the eye.

3.2. Chemical investigation

After growth of the $Fe_{3-x}Cr_xO_4$(111) series, the film stoichiometry was first evaluated *ex situ* by X-ray photoemission spectroscopy (XPS) measurements (**Figure S7**). The *x* values were determined by the relative intensities between the Cr 2*p* (~580 eV) and Fe 2*p* (~720 eV) core-level after Shirley background subtraction, as depicted in the representative XPS spectrum of $Fe_{2.3}Cr_{0.7}O_4$ (bottom left **Figure 2**). Since XPS probes only the surface (top 5-10 nm), complementary chemical analyses were performed by STEM electron energy-loss spectroscopy (STEM-EELS) and STEM energy dispersive X-ray spectroscopy (STEM-EDX). Those analytical techniques presented similar trends with minimal fluctuations in the Fe and Cr signals throughout the layers and no composition gradient (**Figure S8**) is observed. Because these measurements are focused on localized regions, several areas were probed for each sample to assure the homogeneity of our films. **Figure 2** (bottom middle and right) depicts the average STEM-EELS and STEM-EDX spectra for $x = 0.7$, which yield a relative composition of 29 ± 3% of Fe, 7 ± 1% of Cr and 63 ± 3% of O and 34 ± 2% of Fe, 10 ± 2% of Cr and 56 ± 2% of O, respectively. For comparison's sake, the nominal composition (*x* values) of the films were also determined using only the ratio between %Fe and %Cr measured for each technique. As shown in top **Figure 2**, a good agreement in the quantification of Fe and Cr elements was found between the STEM-EELS, STEM-EDX and core level spectroscopies within an error of ~10% of the absolute composition. Hence, we are able to control perfectly the composition of our films and the *x* values obtained via XPS were used for all further analyses.

Besides probing the Fe:Cr ratio in the $Fe_{3-x}Cr_xO_4$(111) series, chemical analyses were also used to investigate the oxidation state and local environment of these cations. The components of the $Fe_{3-x}Cr_xO_4$ spinel layers depict very similar Cr 2*p* and Fe 2*p* XPS spectra with the Cr content (**Figure S7**). This observation is expected for Cr 2*p* XPS spectra as this cation is supposed to have formal charge 3+ and sits in octahedral sites in all compounds. But for Fe 2*p*, the slight differences observed in the spectra are more surprising, even though the Fe^{2+} and Fe^{3+} cation number ratio changes with composition (*e.g.,* 1:2 in Fe_3O_4 and 1:1 in Fe_2CrO_4). In magnetite, Fe 2*p* spectrum is usually interpreted as a complex mix of Fe^{2+} and Fe^{3+} multiplet peaks partially overlapped [44]. It shows a large Fe $2p_{3/2}$ envelope at 710 eV with a shoulder on the low-binding energy side that is specific of a mixed valence iron oxide. Although the presence of overlapping multiplets makes it difficult to proper distinguish the two species, the large peak at 711.2 eV is usually assigned to Fe^{3+} whereas the shoulder at 709.0 eV is primarily a Fe^{2+} contribution. The relative intensities of the multiplets related to Fe^{2+} and Fe^{3+} components will depend on the cation distribution within the near surface. In the case of our iron-chromium spinels, an Fe^{2+} signature (~709.0 eV) lower than expected can be therefore interpreted as an over oxidation of the surface as *x* increases.

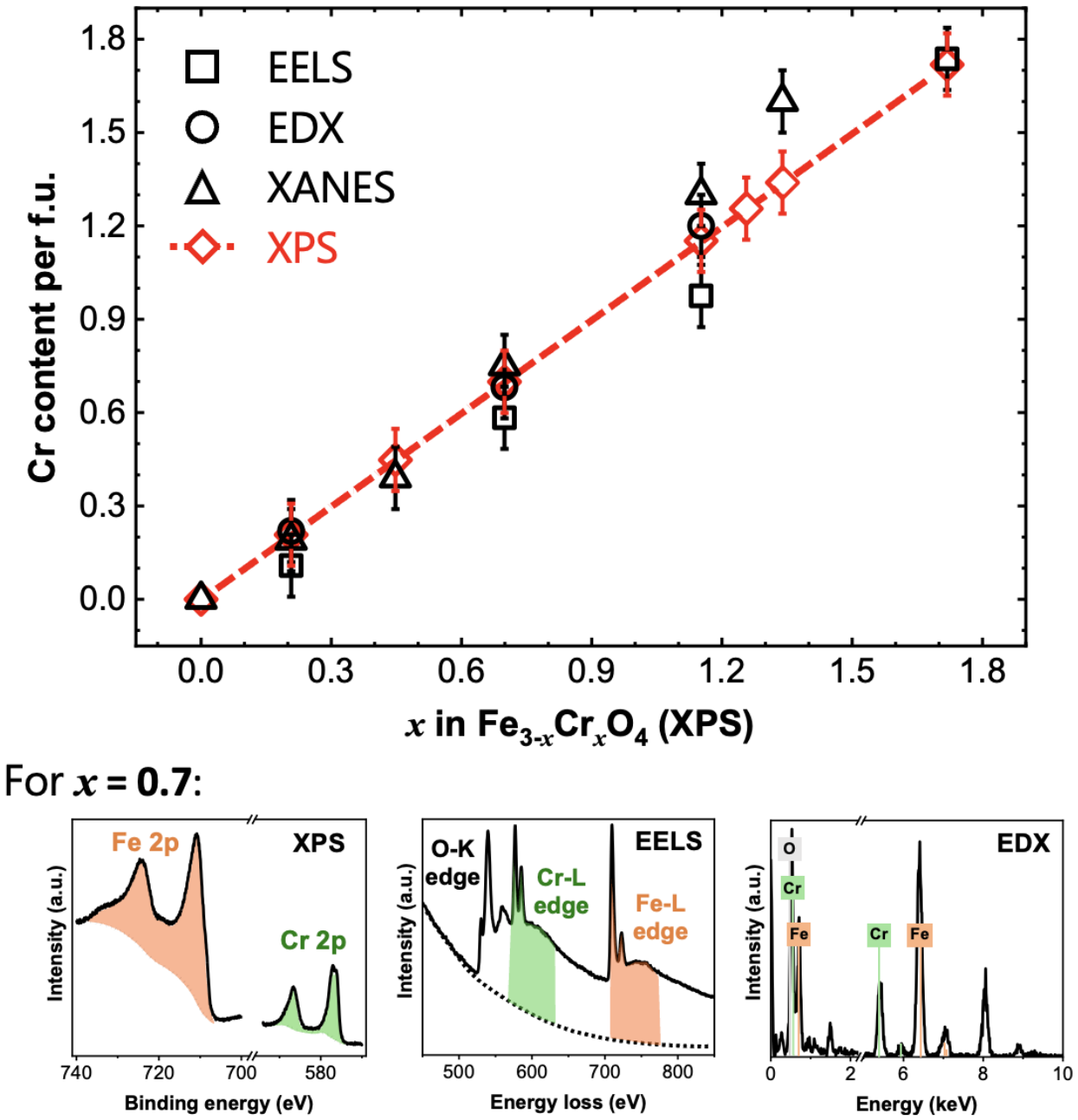

Figure 2. Nominal composition (*x* values) obtained from STEM-EELS (squares), STEM-EDX (circles) and Fe K-edge and Cr K-edge XANES (triangles) analyses in comparison with *x* values extracted from the relative intensity of Fe 2*p* and Cr 2*p* XPS spectra (red diamonds). At bottom, the spectra form and background treatment of XPS in comparison with STEM-EELS and STEM-EDX for $x = 0.7$.

Assessing stoichiometry of the films is a very important step since the oxidation state of the cations can change structural and physical properties of $Fe_{3-x}Cr_xO_4$ [45,46]. To further investigate this matter, X-ray absorption near-edge structure (XANES) analyses were performed on Fe K-edge and Cr K-edge. These spectra (**Figure S9**) show a clear reduction of the average Fe redox as the Cr content in the spinel series increases. We observe a shift of the edge jump and the pre-edge centroid positions

to lower energies for higher *x* values. The analysis of the pre-edge spectral signatures shows that both Fe^{2+} and Fe^{3+} species are presented at Td and Oh-sites in all films (**Figure S10**). For $x < 0.5$, Fe^{2+} contributions (~7113.2 eV) are not pronounced, so these cations occupy mainly Oh-sites. As *x* increases the signal intensity at ~7113.2 eV increases, which indicates that part of the Fe^{2+} ions are displaced to Td-sites. However, none of the analyzed samples has Fe^{2+} ions exclusively at Td-sites, since this signal is not yet very intense. The same can be conclude from Fe K-edge and Cr K-edge EXAFS results (**Table S1**), where the decrease of M_{Oh}–M_{Oh} (M = Fe, Cr) and the increase of M_{Oh}–Fe_{Td} bond lengths suggests that larger Fe^{2+} ions are displaced from Oh to Td-sites as the Cr content increases. The average Fe redox estimated from the XANES edge energy position are in good agreement with the expected for $Fe_{3-x}Cr_xO_4$ (within an average error of 1%). The only exception is $Fe_{1.6}Cr_{1.4}O_4$ that shows Fe redox value 5% lower (+2.26) than expected (+2.38). This means that the sample is slightly under oxidized, which justifies the considerable difference found between XANES and the *x* value determined by XPS (top **Figure 2**). Therefore, thin films with $x < 1.4$ are stoichiometric and the unexpected depletion of Fe^{2+} observed earlier by XPS is rather due to a difference in the cation distribution in the films near surface than an over oxidation of the films with higher Cr content.

Once we have probed the structural quality and stoichiometry of the $Fe_{3-x}Cr_xO_4$ layers for each Cr doping, we then study the relationships between Cr content and physical properties.

3.3. Magnetic behavior and electrical transport

A primary effect of replacing Fe^{3+} with Cr^{3+} in the $Fe_{3-x}Cr_xO_4$ thin films is to change the average magnetic moment on the Oh-sites and the magnetic interactions between Td-Oh and Oh-Oh sites. At first, we assume that the spins on Td-sites of $Fe_{3-x}Cr_xO_4$ are coupled antiferromagnetically to spins on Oh-sites, in the same way as in the magnetite structure (Néel model [42,47]). If we estimate the spin moments from the formal charges of each specie (Cr^{3+}: $3d^3 \rightarrow 3\ \mu_B$, Fe^{3+}: $3d^5 \rightarrow 5\ \mu_B$, and Fe^{2+}: $3d^6 \rightarrow 4\ \mu_B$), thus neglecting the orbital contributions to the total moment, the general composition can be written as $(Fe^{3+}_yFe^{2+}_{1-y})[Fe^{2+}_yFe^{3+}_{2-x-y}Cr_x]O_4$ and the corresponding magnetic moment is $2(3-x-y)\ \mu_B$ per formula unit (f.u.). Based on this idealized structure, the local magnetic moment should exhibit values ranging from $2(3-x)$ to $2(2-x)\ \mu_B$ per f.u., depending on the distribution of Fe^{2+} and Fe^{3+} cations among the spinel sublattices. The upper bound corresponds to the normal spinel configuration, $(Fe^{2+})[Fe^{3+}_{2-x}Cr_x]O_4$, while the lower bound corresponds to a complete inverse spinel configuration, $(Fe^{3+})[Fe^{2+}Fe^{3+}_{1-x}Cr_x]O_4$. Because we are replacing Fe^{3+}_{Oh} ($\mu = 5\ \mu_B$) by Cr^{3+}_{Oh} ($\mu = 3\ \mu_B$), the magnetic moment should decrease linearly with composition (*x*) if the spinel oxide has the same inversion parameter (*y*).

In order to comprehend the effect of increasing Cr content on the magnetic properties of $Fe_{3-x}Cr_xO_4$ samples, in-plane magnetic hysteresis loops (**Figure 3a**) were recorded using a vibrating-sample magnetometer (VSM). They were studied at room temperature up to a magnetic field of 2 Tesla applied along the $[11\bar{2}0]$ axis of the α-Al_2O_3 substrate. In general lines, the $Fe_{3-x}Cr_xO_4$ thin films exhibited easy in-plane magnetization for x up to 1.4. The saturation magnetization (M_S) and remanent magnetization (M_R) decrease as x increases. While M_S values (**Figure 3b**) ranged from 280 kA m^{-1} to 90 kA m^{-1} for $0 < x < 1.4$, M_R (not shown) reached from 38% to 15% of the magnetization at 1.5 Tesla for this same range of x values. The observed coercive field (**Figure 3b**), $\mu_0 Hc$, also decreased with x, ranging from 0.040 Tesla ($x = 0$) to 0.012 Tesla ($x = 1.4$), except for $x = 0.5$, which show a high $\mu_0 Hc$ of 0.046 Tesla. Note that both Ms and $\mu_0 Hc$ do not evolve linearly with composition, which is most probably due to changes in the inversion parameter (y). Another point is that the magnetic moment measured for Fe_3O_4 (2.3 μ_B per f.u.) is considerably lower than the bulk value of 4.2 μ_B per f.u. This can be explained by the presence of APBs (**Figure 1b2**) since the magnetic coupling across an APB is rather antiferromagnetic [48], which may reduce the average magnetic moment of the thin film. This phenomenon has been widely studied for magnetite[42,49] and also affects the magnetic properties of all our $Fe_{3-x}Cr_xO_4$ series. Indeed, the M_S values are consistently lower than lower bound on the magnetic moment corresponding to an inverse spinel configuration, *i.e.*, 4 μ_B per f.u. for $x = 0$ and 1.2 μ_B per f.u. for $x = 1.4$.

Another effect of substitutional Cr in the Fe_3O_4-$FeCr_2O_4$ system is the modification of the conduction mechanism, since the former is a known half-metal material while the latter is an insulator. In ferrites, the electron conductivity is associated to the easy electron transfer in Oh-sites and requires two critical steps to occur: 1) the presence of charge carrier donor/acceptor pairs ($M^{n+}/M^{(n+1)+}$) and 2) enough energy to overcome the activation barrier between hopping pairs [50]. Assuming that the charge transport occurs predominantly between like-cation pairs, only Fe^{2+}/Fe^{3+} pairs should participate in electron hopping in this system as Cr assumes only one oxidation state. Hence, on replacing a Fe^{3+} cation with a Cr^{3+} cation in Oh-sites, we expect those charge-conducting sites to be blocked and the charge transport to be affected by the increase in hopping barriers. In addition, if Fe^{2+} cations are displaced to Td-sites, as suggested by structural and chemical analyses, a new conduction mechanism involving hopping between Td and Oh-sites should also be considered [51,52].

Figure 3c shows the resistivity of $Fe_{3-x}Cr_xO_4$ thin films as function of the temperature measured using standard four-probe method in a quantum design physical properties measurement system (PPMS). For all compositions, the expected semiconducting behavior with increasing resistivity for decreasing temperature is clearly observed. Moreover, there is a general increase in the resistivity of spinel solid solution with higher x content, consistent with the decrease in the total

number of conducting Fe^{2+}/Fe^{3+} pairs. For instance, the resistivity of the films at room temperature ranged from 7×10^{-4} Ω m for Fe_3O_4 to 1×10^{-1} Ω m for $Fe_{1.8}Cr_{1.2}O_4$, increasing gradually with the Cr content. No abrupt drop of conductivity (typical of the Verwey transition) was observed upon cooling for $Fe_{3-x}Cr_xO_4$. Since Cr^{3+} ions disrupt the electron hopping along Oh-sites, introducing Cr into the magnetite structure inhibits the Verwey transition as it requires long-range ordered Fe^{2+}_{Oh}-Fe^{3+}_{Oh} [53]. Note that the resistivity measured for Fe_3O_4 is considerably higher than the bulk value of 4×10^{-5} Ω m. As for the saturation magnetization, this can also be explained by the presence of APBs (**Figure 1b2**), which act as scattering centers hindering the electron transport across the films [25]. Moreover, as aforesaid, the magnetic coupling across an APB is rather antiferromagnetic [48] while the charge transfer in Fe_3O_4 requires ferromagnetic alignment between neighboring donor/acceptor pairs. The presence of APBs thus affects the conductivity of all our $Fe_{3-x}Cr_xO_4$ series.

In order to investigate the conduction mechanism governing our system, we considered the general charge transport equation:[54]

$$\rho(T) = \rho_0 \times T^m \times e^{(E_a/k_BT)^p},$$

where pre-factor ρ_0 is the resistivity at $T \rightarrow \infty$ related to the concentration of donor/acceptor pairs. E_a is the activation energy associated with electron hopping, k_B is Boltzmann's constant, T is temperature, p and m are constants. The exponent m gives the type of electrons conduction, with m = 1 in the case of small polarons hopping conduction and m = 0 in the case of band conduction. Meanwhile, the power-law dependence (p) gives the type of charges hopping, *e.g.* p = 1 corresponds to nearest-neighbor hopping (NNH) and p = 0.5 (or 0.25) to variable range hopping (VRH) [55]. Based on the least-squares fitting of the Arrhenius curves (**Figure 3c**), we deduced that the electronic transport of the $Fe_{3-x}Cr_xO_4$ series satisfies the NNH mechanism with $m = p = 1$ at the measured temperature ranges (*i.e.*, above Verwey transition for Fe_3O_4).

The values of ρ_0 and E_a extracted from the NNH mechanism (**Figure 3d**) are clearly affected by the increase of Cr content. The pre-factor ρ_0 steadily increases from 4.0×10^{-5} Ω m (x = 0) to 1.7×10^{-4} Ω m (x = 1.2), while the activation energy E_a increases from 76 meV (x = 0) to 161 meV (x = 1.2). The material hence shows a more insulator-like behavior with increasing Cr content. The monotonic increase of activation energy with composition confirms that Cr is not active in the transport process for $x < 1.2$, which is in good agreement with the conduction mechanism proposed for $Fe_{3-x}Cr_xO_4$ bulk samples [21]. Using a simple hopping model [56], ρ_0 can be related to Fe^{2+}/Fe^{3+} pair concentration and the possibility of this pair to form a conductive pathway. Therefore, in order to understand the evolution of the conduction mechanism with Cr content, it is mandatory to determine precisely the cation site-occupation, as discussed in the next sections.

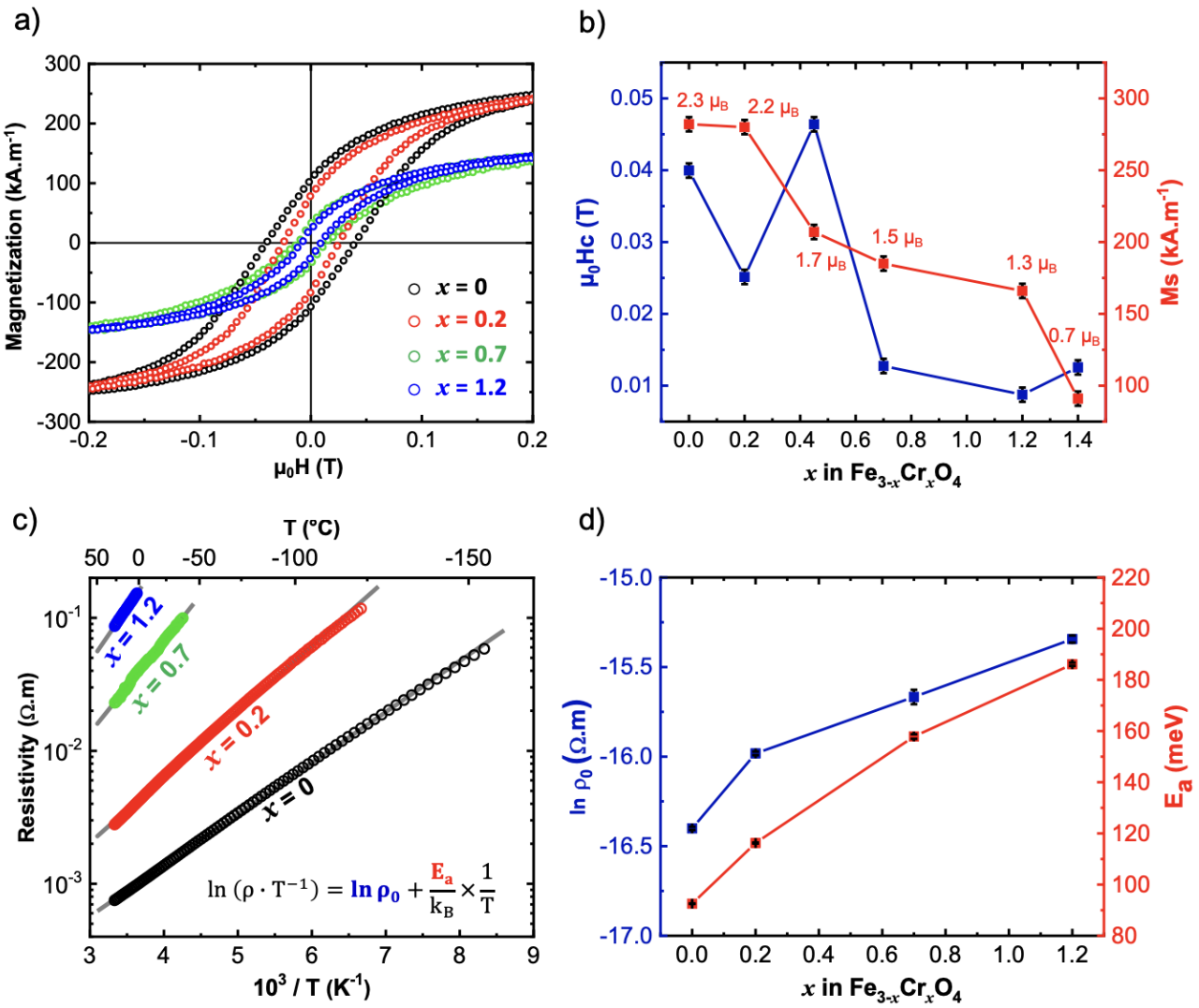

Figure 3. Magnetic behavior and electronic transport in $Fe_{3-x}Cr_xO_4$ thin films. (a) In-plane magnetic hysteresis loops for x = 0 (black), x = 0.2 (red), x = 0.7 (green) and x = 1.2 (blue) at T = 300 K. (b) Coercive field $\mu_0 Hc$ (left y-axis) and saturation magnetization Ms (right y-axis) acquired at 1.5 Tesla for the respective film compositions. (c) Temperature-dependent resistivity plotted as Arrhenius curve for $Fe_{3-x}Cr_xO_4$ thin films. Inset, the small-polaron band transport equation. (d) The pre-factor ρ_0 (left y-axis) and the activation energy Ea (right y-axis) extracted from the fit of the Arrhenius curves. The error bars included in the plot are calculated based on the least-squared minimization linear fitting, which were consistently smaller than 1% for all samples.

3.4. Fine structure investigation

To comprehend thoroughly the evolution of the physical and chemical properties discussed in the previous sections, the cationic site distribution in our $Fe_{3-x}Cr_xO_4$ thin films was quantified via X-ray absorption spectroscopy (XAS) and X-ray magnetic circular dichroism (XMCD) measurements at Cr and Fe $L_{2,3}$-edges. The XMCD spectra result from the difference between XAS spectra recorded

with circularly right and left polarizations at a given absorption edge for a sample exposed to a magnetic external field parallel to the beam. An assessable XMCD signal is associated with a non-zero magnetic moment along the light propagation axis. More precisely, the XMCD signal here is related to the presence of a ferromagnetic or ferrimagnetic long-range order. **Figure 4** shows the XAS (upper panel) and XMCD (lower panel) spectra of two representative $Fe_{3-x}Cr_xO_4$ thin films (x = 0.2 and 1.2). Spectra of all compositions (and detailed simulations) are depicted in Supporting Information (**Figure S11-S14**).

The Cr $L_{2,3}$-edges XAS and XMCD spectra (**Figure 4a**) are divided in the spin-orbit split L_3 (~577 eV) and L_2 (~585 eV) parts. According to Crystal Filed Multiplet (CFM) calculations, the entire curves can be described properly using only Cr^{3+} ion with the $3d^3$ ionic configuration and the O_h symmetry group (**Figure 4a**, red line). They therefore confirm that Cr^{3+} ions replace Fe^{3+} ions exclusively at Oh-sites of the spinel structure. The Fe $L_{2,3}$-edges XAS and XMCD spectra (**Figure 4b**) are also divided in the spin-orbit split L_3 (~707 eV) and L_2 (~720 eV) parts and display the multiplet structure typical of the ionic nature of iron. In this case, only one symmetry cannot describe the entire Fe spectra and CFM calculations were performed considering both O_h and T_d symmetry groups. According to them, the Fe L_3-edge can be decomposed in four distinct contributions:

A. the peak at 705.5 eV comes mainly from Fe^{2+} at Td-sites (blue area);
B. the one at 706.2 eV comes from Fe^{2+} (green area) and Fe^{3+} (pink area) ions at Oh-sites;
C. the peak at 707.3 eV comes exclusively from Fe^{3+} ions at Td-sites (yellow area);
D. the one at 708.0 eV is linked to Fe^{3+} ions at Oh-sites.

The Fe_{Td} and Fe_{Oh} (or Cr_{Oh}) contributions in the XMCD spectra have opposite sign, confirming the ferrimagnetic order with an antiparallel alignment between magnetic moments in Td and Oh-sites. In this study, the XMCD measurements were carried out in saturated magnetic field (*i.e.*, 2 Tesla), so that spins are aligned to the magnetic field and the magnetization can be determined quantitatively. The size of the Fe $L_{2,3}$-edges (or Cr $L_{2,3}$-edges) XMCD signal reduced as the Cr content increased: from 35% of the XAS signal for $Fe_{2.8}Cr_{0.2}O_4$ to only 7% of the XAS signal for $Fe_{1.8}Cr_{1.2}O_4$. Therefore, the total magnetic moment diminishes with the insertion of Cr in the magnetite structure and the films become more paramagnetic, as observed by VSM measurements (**Figure 3b**).

The cationic site distribution of $Fe_{3-x}Cr_xO_4$ was determined so that the weighted sum of each calculated contribution reproduces the intensity and shape of the dichroic experimental spectra (**Figure 4b**, red line). **Figure 5a** summarizes the Fe and Cr cation distribution on Td and Oh-sites derived from the best fit with the measured Fe $L_{2,3}$-XMCD spectra. For $x \leq 0.5$ (region I), very little

(or none) Fe^{2+}_{Td} contribution is observed. The Fe^{3+}_{Oh} contributions steadily decrease as the Cr^{3+}_{Oh} molar fraction increases, while Fe^{3+}_{Td} and Fe^{2+}_{Oh} species keep a ratio of 3:4. In this region, Cr^{3+} mostly replaces Fe^{3+} ions at Oh-sites without changing the spinel configuration. For $x > 0.5$ (region II), however, Fe^{2+}_{Td} molar fraction increases, while Fe^{3+}_{Oh} contributions changes little. Thus, each added Cr^{3+} displaced one Fe^{2+} from Oh-sites, thereby changing the spinel configuration. To sum up, $Fe_{3-x}Cr_xO_4$(111) thin films show two different configurations depending on the Cr content: (*i*) mainly inverse spinel $(Fe^{3+})[Fe^{2+}Fe^{3+}_{1-x}Cr_x]O_4$ for $0 < x < 0.5$ and (*ii*) intermediate spinel $(Fe^{3+}_yFe^{2+}_{1-y})[Fe^{2+}_yFe^{3+}_{2-x-y}Cr_x]O_4$ for $0.5 < x < 1.2$ with $0.9 < y < 0.5$. These findings are in overall good agreement with both structural and chemical analysis previously shown as well as Mossbauer measurements [15,57] performed on bulk samples (**Figure 5a**, dashed black lines), which predicted that this series varies from an inverse arrangement ($y = 1$) to a normal ordering ($y = 0$) when x goes from 0 to 2 (**Figure 5b**, dashed green lines). However, the transition from one spinel configuration to another is less abrupt in our films than in the bulk. As depicted in **Figure 5b**, our films remained intermediate spinel for x up to 1.2, while bulk samples are almost a complete normal spinel for such composition. Here the inversion parameter y is deduced from the tetrahedral contributions ($y = M_{Fe^{3+}_{Td}}/M_{Fe^{2+}_{Td}} + M_{Fe^{3+}_{Td}}$) as the Fe^{2+}_{Oh} contributions are generally overestimated in our fits.

It is noteworthy that the XAS (or XMCD) quantitative analysis has an absolute uncertainty of about 10%. The inclusion of Fe^{2+}_{Td} contributions up to 5% does not change significantly the quality of the fit for $x \leq 0.5$, which constitutes the error bars shown in **Figure 5a**. Thus, small amounts of Fe^{2+} can be included at Td-sites for these compositions, so that the spinel structure is not in a perfect inverse arrangement, but with an inversion parameter between 90 to 100%, as observed elsewhere [15]. Moreover, we noticed a Fe^{3+}_{Td} : Fe^{2+}_{Oh} ratio of 3:4 instead of 1:1 as in an ideal spinel structure, which may be due to imperfections of the model fit. In fact, the model used here is simple, since it does not account for charge transfer effects nor distortions in the cation local symmetry. The choice of a simpler model was made due to its robustness and the smaller number of parameters considered in the fit. Another explanation is the presence of surface defects. The total electron yield detection mode used to record the XMCD spectra is rather surface sensitive in the soft X-ray regime [58], unlike other techniques, such as K-edge XANES (**Figure S9**-**S10**), used here to probe the stoichiometry and cation redox of the entire thin film.

After this thorough analysis of the evolution of the spinel structure, we undertook to establish the link between the cation site distribution and the physical properties.

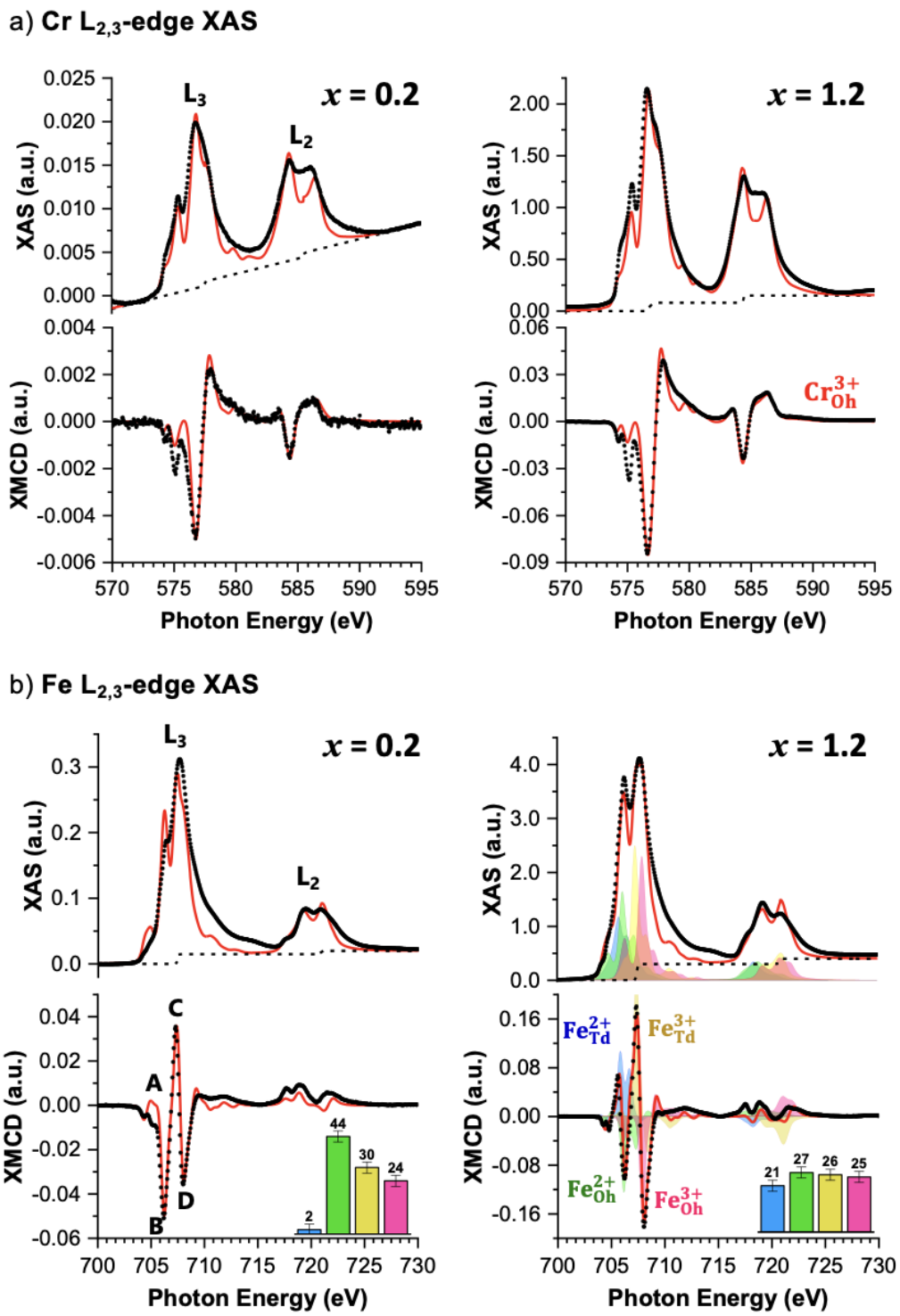

Figure 4. Fine structure characterization of $Fe_{3-x}Cr_xO_4$ thin films. Experimental (a) Cr and (b) Fe $L_{2,3}$-edges XAS (top) and XMCD (bottom) spectra measured at B = 2.0 T and at room temperature. To facilitate comparison with calculations, which themselves have no background, the raw spectra were normalized to the pre-edge and the background constant to 1 was subtracted. After this operation, step-like backgrounds (dashed lines) were traced. The calculated contribution for each iron species is shown in the right bottom spectra: $Fe^{2+}{}_{Td}$ (blue), $Fe^{2+}{}_{Oh}$ (green), $Fe^{3+}{}_{Td}$ (yellow) and $Fe^{3+}{}_{Oh}$ (pink). The red line depicts the sum of the cation contributions calculated by CFM. In inset, the distribution of Fe species (in %).

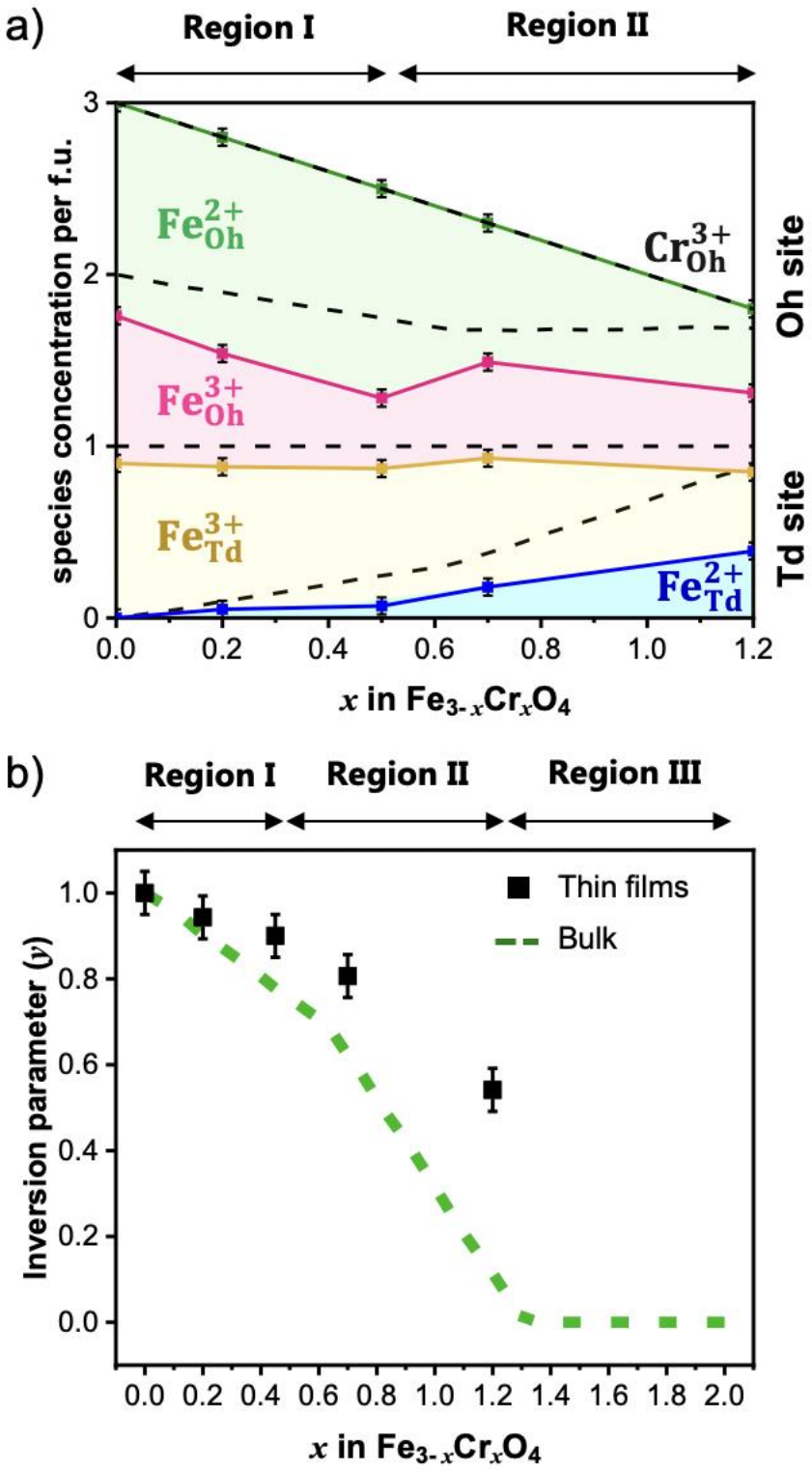

Figure 5. (a) Site distribution diagram of the species concentrations from XMCD measurements (solid lines), in comparison with values for bulk structure [15] (dashed black lines). (b) The evolution of the inversion parameter (y) with composition (x) for thin films (black squares) and bulk[15] (dashed green line).

3.5. Macroscopic behavior from the fine structure perspective

First, we discuss the impact of the cation distribution in the magnetic properties of $Fe_{3-x}Cr_xO_4$(111) thin films. **Figure 6a** compares the total magnetic moment (μ_{total}) obtained from VSM measurements (**Figure 3a**) for thin films with the bulk values shown in the literature [15,59]. Here the thin film values decreased more smoothly with composition *x* than for the bulk. Whereas bulk μ_{total} dropped sharply from 3.8 to 0.3 μ_B per f.u. within the composition range of $0 \leq x \leq 1.2$, the film values decreased gently from 2.2 to 1.3 μ_B per f.u. within the same range and then dropped to 0.7 μ_B per f.u. for $x = 1.4$. Note that films with high Cr content ($x \geq 1.2$) show higher magnetic moments ($\mu_{total} > 0$) than the bulk. This is due to differences in the inversion parameter (*y*) observed in **Figure 5b**. To delve deeper into this issue, **Figure 6a** (open black squares) shows the expected average magnetic moment calculated from the *y* values deduced from the Fe XMCD fits. According to the XMCD measurements, the Oh-site moments align parallel to one another and antiparallel to the Td-site moments, as observed in other Cr containing spinels [60,61]. Assuming that formal charges can be used to estimate the spin moments of each specie, the corresponding magnetic moment is $2(3-x-y)$ μ_B per f.u., as aforementioned. As depicted in **Figure 6a**, the local magnetic moment deduced from the cationic site distribution decreases gradually with Cr content. Although they evolve with composition in a similar way than the VSM measurements, they are shifted to higher values due to the presence of APBs.

Finding a similar evolution of the magnetic moments measured by VSM compared to those deduced by the Néel model implies that the Fe and Cr moments are mostly collinear in the thin films. Unlike bulk samples, for which the Néel model is valid only for *x* up to 0.5 [13,15,59], in thin films, this model is apparently valid for further compositions. This is because the thin films maintained an intermediate spinel configuration with higher inversion parameter for larger Cr content. According to Néel [47], in spinel oxides each ion experiences a field due to the ions on both spinel sublattices, so magnetic properties of this ferrimagnet depends on the strength of inter (Td-Oh) and intra (Td-Td and Oh-Oh) sublattice exchange interactions. Increasing the amount of Fe^{2+} displaced at Td-sites (*i.e.*, to decrease *y*) weakens the Td-Oh antiferromagnetic interactions in the spinel structure. Likewise, increasing the amount of Cr^{3+} in Oh-sites increases the strength of the next-nearest neighbor Oh-Oh antiferromagnetic interactions. Depending on the competing force of these interactions, they may tilt the cation spin moments in the spinel sublattices. Therefore, the local magnetic moment should decrease proportionally to the amount of Fe^{2+} ions displaced to Td-sites and Cr^{3+} ions occupying Oh-sites. For bulk samples, the Néel model is valid for *x* up to 0.5, whose inversion parameter is 0.75. Since the thin films keep a higher inversion parameter of 0.80 for *x* up to 0.7, the Néel model should

indeed be valid up to this film composition. On the other hand, y = 0.5 for x = 1.2, so for this composition the spin moments of Cr^{3+} ions are slightly canted.

In addition to increasing the local magnetic moment, more intense Td-Oh antiferromagnetic interactions should also increase the Curie temperatures of $Fe_{3-x}Cr_xO_4$ with higher Cr content. In bulk samples (**Figure 6b**, dashed blue line), we observe that T_C decreases as x increases, so that compounds having $x > 1.2$ become ferrimagnetic only below room temperature. Note that T_C decreases slightly for limiting compositions ($x < 0.5$ and $x > 1.5$), while for intermediate compositions ($0.6 < x < 1.2$) T_C decreases rapidly with increasing values of x. The sharp decrease in Curie temperature is related to the decrease in the inversion parameter from 0.7 to 0 in this same compositional range. In fact, the presence of Fe^{3+} on both Td and Oh-sites leads to strong Td-Oh antiferromagnetic interactions that are responsible for the high Curie temperatures of inverse spinel ferrite. **Figure 6b** shows Curie temperatures calculated using the inversion parameter of thin films (black squares) in comparison with the one of bulk samples (green circles). According to these atomistic spin simulations, T_C values of the $Fe_{3-x}Cr_xO_4$ series increase sharply with the increase of the inversion parameter. For example, the increase of inversion parameter from 0.1 to 0.5 leads to a considerable increase in T_C from 305 K to 480 K for x = 1.2, which explains why this sample still showed magnetization at room temperature, *i.e.*, near the Curie temperature of bulk samples.

Another factor contributing to the higher T_C values for lower Cr-content is the occurrence of electron transfer from $Fe^{2+}{}_{Oh}$ to $Fe^{3+}{}_{Oh}$ ions. The charge hopping provides an additional ferromagnetic interaction through double exchange, which helps to overcome the antiferromagnetic Oh-Oh interactions. Like the magnetic properties, the electron transfer is also closely related to the cation distribution. Indeed, three types of pathways for electron hopping (**Figure 7a**) can be considered if Fe^{2+} populates both sublattices, as described by the general formula: $Fe_a^{2+} + Fe_b^{3+} \rightarrow Fe_a^{3+} + Fe_b^{2+}$. The first one is Oh-to-Oh site hopping, which is the favored mechanism in the spinel structure since the Oh-sites form infinite edge-sharing networks with one another. The other ones are Td-to-Td and Td-to-Oh transfer. These mechanisms are usually rejected for spinel ferrites since they are unfavorable over the Oh-to-Oh transfer [21]. In the spinel structure, the Td-sites share corners with Oh-sites, but are isolated from one another. The existence of a large number of pairs of close neighbor states is essential for the NNH conduction to occur. Moreover, contrary to the case of Fe^{2+} and Fe^{3+} octahedra sharing edge, the t_{2g} atomic orbitals of the two ions overlap poorly for Fe^{2+} and Fe^{3+} sharing corners thereby hindering electron transfer between Td and Oh-sites. Although octahedral hopping appears to dominate in spinels, it may become invalid if the system is disordered or non-stoichiometric [51].

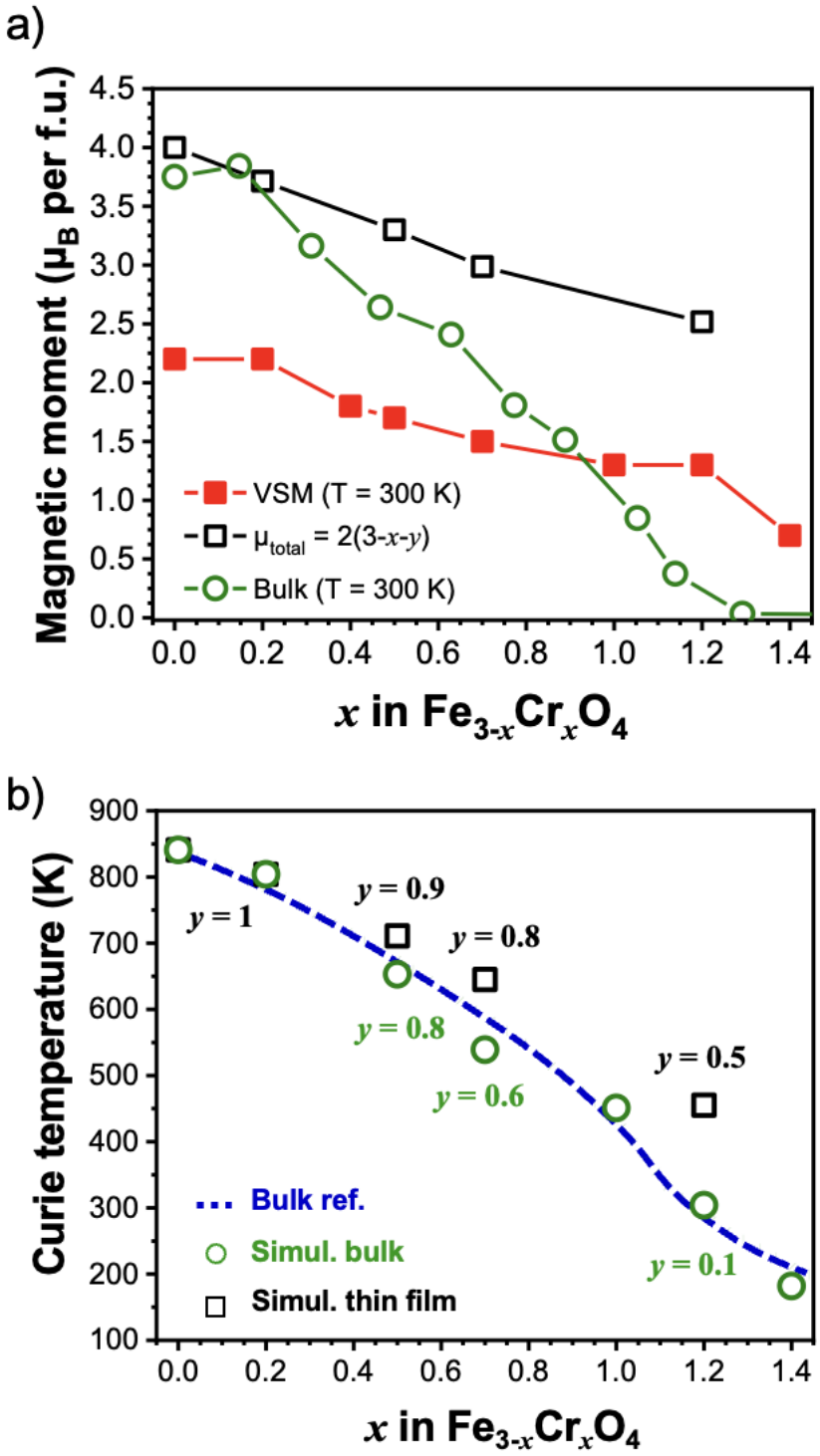

Figure 6. From cation site distribution to the magnetic properties of $Fe_{3-x}Cr_xO_4$ thin films. (a) Evolution of local magnetic moment with composition for bulk samples [59] (green circles) in comparison with thin films (VSM measurements in red and values deduced from the cation site distribution in black) at room temperature. (b) Calculated Curie temperature (black squares) for $Fe_{3-x}Cr_xO_4$ thin films in comparison with bulk samples (experimental data in dashed blue line and values calculated from the cation distribution in green circles). Herein, the error bars are the size of the point (~1%).

If small polaron approximation is considered, the electrical conductivity (σ) [21,52], which is the inverse of resistivity (ρ), is given by:

$$\sigma = \frac{Nc'(1-c')ga^2e_0^2\nu_0}{k_BT} e^{(-E_H/k_BT)},$$

where g is a geometric factor that is constant for a given system, a is the jump length, v_0 is the lattice vibration frequency, N is the density of conducting sites, c' is the fraction of conducting sites occupied by charge carriers, (1-c') is the fraction of potential jump sites, E_H is the hopping energy, and the remaining terms have their usual meaning. Here the probability that there are enough M^{n+}/ $M^{(n+1)+}$ components aligned in a contiguous pathway for percolation to occur is given by $Nc'(1-c')$. The behavior of electrical conductivity can be then predicted from the knowledge of the content and distribution of Fe^{2+} cations amongst Oh and Td occupied sites (*i.e.*, the inversion parameter y). For instance, considering Oh-to-Oh transfer, $c' = Fe^{2+}_{Oh} / (Fe^{2+}_{Oh} + Fe^{3+}_{Oh})$, $1-c' = Fe^{3+}_{Oh} / (Fe^{2+}_{Oh} + Fe^{3+}_{Oh})$, and N becomes the total concentration $Fe^{2+}_{Oh} + Fe^{3+}_{Oh}$. Hence, $Nc'(1-c')$ is written as $(Fe^{2+}_{Oh} \times Fe^{3+}_{Oh})/(Fe^{2+}_{Oh} + Fe^{3+}_{Oh})$. In the same way, $Nc'(1-c')$ is equal to $(Fe^{2+}_{Td} \times Fe^{3+}_{Oh})/(Fe^{2+}_{Td} + Fe^{3+}_{Oh})$ for Td-to-Oh transfer and $Nc'(1-c')$ is equal to $(Fe^{2+}_{Td} \times Fe^{3+}_{Td})/(Fe^{2+}_{Td} + Fe^{3+}_{Td})$ for Td-to-Td transfer.

First, the small polaron approximation is used to understand the electron hopping on bulk samples. **Figure 7b** shows the evolution of concentration of hopping pairs, $Nc'(1-c')$, as function of x considering the bulk cation distribution [15,57] (dotted lines) and the XMCD results for our $Fe_{3-x}Cr_xO_4$ thin films (squares). For bulk samples, the probability of $Fe^{2+}_{Oh}/Fe^{3+}_{Oh}$ to form a contiguous pathway is maximum at the equivalence point $Fe^{2+}_{Oh} = Fe^{3+}_{Oh}$ ($x = 0$ and $y = 1$) and then decreases steadily as the Fe_{Oh} percolation pathways are broken by Cr cations and they become inactive. Herein, we assume that Cr do not act as an electron donor or acceptor and is not involved in conduction. For $x > 0.8$, the amount of $Fe^{2+}_{Oh}/Fe^{3+}_{Oh}$ pairs diminish sharply due to the decrease of the inversion parameter until the critical value of $x = 1.3$ ($y = 0$) where there is no possible $Fe^{2+}_{Oh}/Fe^{3+}_{Oh}$ pathway since all Fe^{2+} cations have been displaced to Td-sites. On the other hand, the number of $Fe^{2+}_{Td}/Fe^{3+}_{Oh}$ pathways steadily increase in the $0 < x < 1.3$ range with the decrease of inversion parameter, being maximum at $x = 1.3$ ($y = 0$) where all Td-sites are occupied by Fe^{2+} cations and only 65% of the Oh-sites are blocked by Cr. For $x > 1.3$, the amount of $Fe^{2+}_{Td}/Fe^{3+}_{Oh}$ contiguous pathways drop significantly as they are progressively broken by Cr. Likewise, the concentration of hopping $Fe^{2+}_{Td}/Fe^{3+}_{Td}$ pairs increases until $x = 0.8$ (where $Fe^{2+}_{Td} = Fe^{3+}_{Td} = 0.5$) and then decreases sharply due to the decrease of inversion parameter. Though, the amount of those pairs is never greater than $Fe^{2+}_{Oh}/Fe^{3+}_{Oh}$ or $Fe^{2+}_{Td}/Fe^{3+}_{Oh}$ hopping pairs. Therefore, for bulk samples, the conduction mechanism

will go through Oh-to-Oh site hopping until x = 1.2, whereas the more Cr-rich compositions may exhibit Td-to-Oh hopping or mixed Fe^{2+}-Fe^{3+}-Cr^{3+} electron transfer, as suggested by Nell and Wood [21]. The transition from the Oh-to-Oh to the less favorable mechanism requires an appreciable amount of added energy. Consequently, Nell and Wood[21] observed a rapid increase of the activation energy in the $1.2 < x < 1.5$ region.

For the $Fe_{3-x}Cr_xO_4$(111) thin films, the dominant mechanism in the compositional range studied is Oh-to-Oh site hopping, as they remained intermediate spinel for x up to 1.2. As shown in **Figure 7b**, the amount of the $Fe^{2+}{}_{Oh}/Fe^{3+}{}_{Oh}$ is greater than $Fe^{2+}{}_{Td}/Fe^{3+}{}_{Oh}$ or $Fe^{2+}{}_{Td}/Fe^{3+}{}_{Td}$ hopping pairs for all considered compositions. Moreover, the pre-factor $\rho_{0,exp.}$ determined from the fit of the resistivity curves (**Figure 3d**) can be related to the probability of finding a Fe^{2+}:Fe^{3+} pair in neighbor Oh-sites. In **Figure 7c**, good correlation was found between the calculated ρ_0 ($\rho_0 \propto [Nc'(1-c')]^{-1}$) for Oh-to-Oh hopping path to the experimentally determined pre-factor ($\rho_{0,exp.}$). The same cannot be said for the calculated ρ_0 for Td-to-Oh and Td-to-Td paths, which confirms that the polaron hopping model describes well the Oh-to-Oh electron transport in this ternary system.

Although the electron hopping along the favored Oh-to-Oh site is still possible for x up to 1.2, the probability of hopping along this path is effectively affected by Cr-concentration. As the distance between neighboring Fe^{2+} and Fe^{3+} in Oh-sites increases by the presence of $Cr^{3+}{}_{Oh}$, the electrons are forced to follow narrow and complicated channels to an extent as high as the Cr content. Indeed, ρ(300 K) (**Figure 3c**) increased from 7×10^{-4} Ω m (x = 0) to 3×10^{-3} Ω m (x = 0.2) since 10% of the Oh-sites were blocked by Cr^{3+} cations. Moreover, a monotonic increase of activation energy (**Figure 3d**) was observed for the thin films. As discussed above for bulk samples [21], the absence of sharp increase of activation energy confirms that the octahedral hopping between Fe^{2+} and Fe^{3+} is the sole pathway for the films. Compared to these bulk samples, smaller activation energies were found for higher Cr content films considering the same NNH hopping model. For instance, for x = 1.2, Nell and Wood[21] found E_a = 250 meV, while for thin films E_a = 161 meV. Similar activation energy (E_a = 150 meV) was found for 120 nm thick $Fe_{1.8}Cr_{1.2}O_4$ films grown on MgO(001) [22]. This is due to the greater amount of $Fe^{2+}{}_{Oh}/Fe^{3+}{}_{Oh}$ hopping pairs for both thin films, as they have greater inversion parameter. Moreover, this composition shows slight deviation from stoichiometry, which also contributes to the improvement in the transport properties.

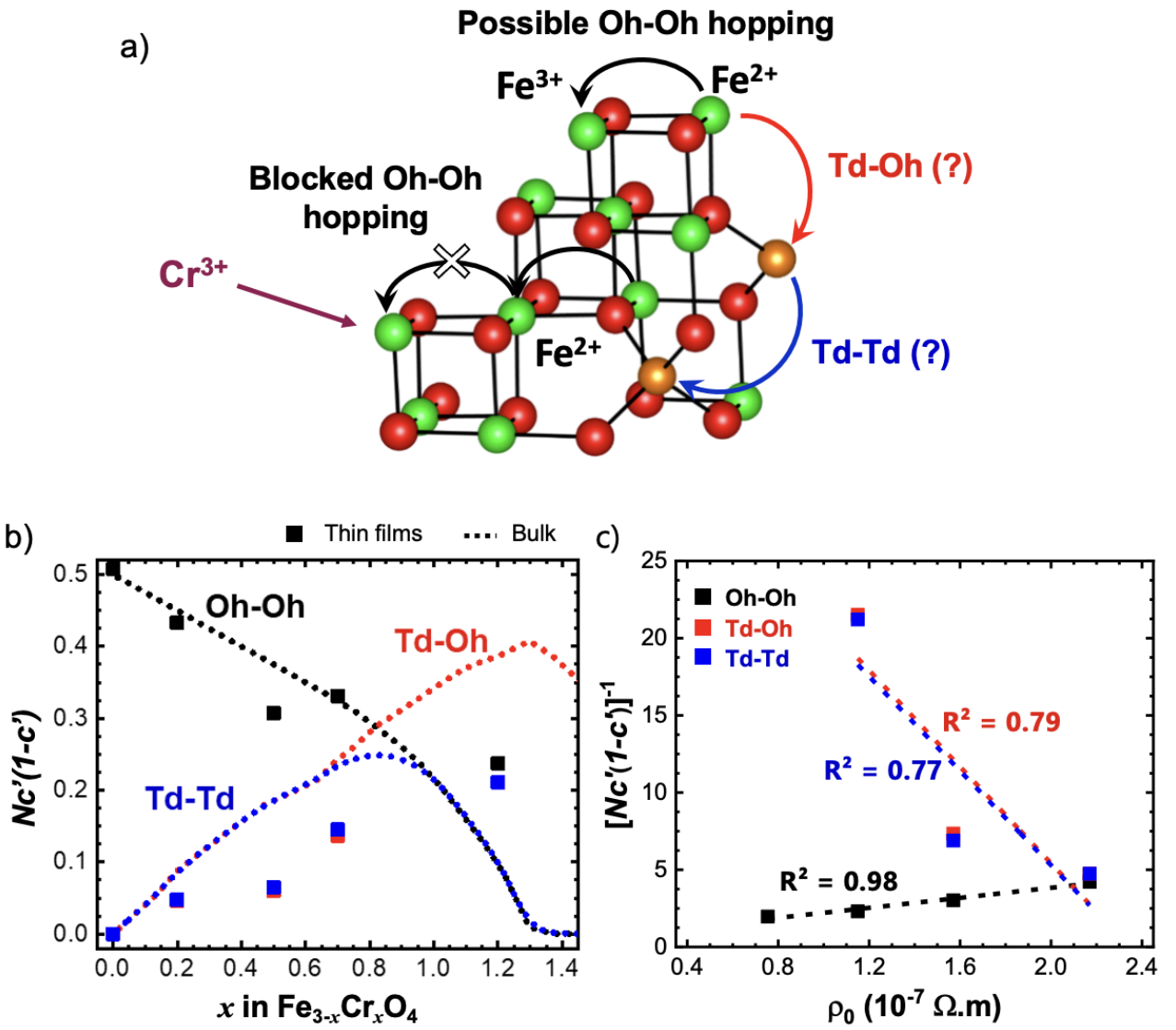

Figure 7. From cation site distribution to the conductivity of $Fe_{3-x}Cr_xO_4$ thin films. (a) Concentration of hopping pairs *Nc'(1-c')* (where c' is the fraction of conducting sites and *N* is the density of conducting sites) for different electron hopping pathways: Oh-to-Oh (black), Td-to-Oh (red) and Td-to-Td (blue), as depicted in (b). Dotted lines represent the values deduced from the bulk cationic site distribution[15] and the squares are the values for the thin films. (c) Comparison of the experimental pre-exponential term of the resistivity measurements (ρ_0) and concentration of hopping pairs considering Oh-to-Oh site hopping.

4. Conclusions

Stoichiometric epitaxial 15 nm thick $Fe_{3-x}Cr_xO_4(111)$ thin films were grown on single crystalline α-$Al_2O_3(0001)$ substrates by O-MBE. For $x \leq 1.2$, the structural analyses evidenced high crystalline quality, low surface roughness and low density of defects. According to XMCD analyses, Cr ions assume exclusively a 3+ oxidation state and sit at Oh-sites for all films, while Fe^{2+} and Fe^{3+}

ions populate both Td and Oh-sites. For $x \leq 0.5$, $Fe_{3-x}Cr_xO_4$ showed mostly an inverse spinel structure with very little Fe^{2+} sitting at Oh-sites. For $x > 0.5$, Fe^{2+} ions are steadily displaced to Td-sites and the spinel shows an intermediate configuration where the inversion parameter steadily decreases as x increases. Moreover, the films showed different behavior than the bulk within the same composition range. Like bulk materials, the total magnetization and the magnetic anisotropy of $Fe_{3-x}Cr_xO_4$ thin films decrease as the Cr content increase. But unlike bulk materials, thin films with high Cr content ($x \geq 1.2$) still showed magnetization at room temperature, *i.e.*, near (or above) the Curie temperature of bulk samples. These features were interpreted in the light of the cationic site distribution. For both bulk and thin films, the inversion parameter steadily evolves with composition, ranging from an inverse arrangement (Fe_3O_4) to normal ordering ($FeCr_2O_4$). However, the transition from one spinel configuration to another is less abrupt in the films than in the bulk. Because thin films with high Cr content are still intermediate spinels, while bulk samples are normal spinels, the Curie temperature of these films were increased as they present stronger Td-Oh antiferromagnetic interactions. These results confirm that doping magnetite thin films with Cr is very effective to control the magnetic behavior of this material.

Besides changing the magnetic properties of the material, the cation distribution also plays a key role in the conduction behavior. The electron pathways in $Fe_{3-x}Cr_xO_4$(111) thin films were found to be the same as the nearest-neighbor Oh-site hopping in magnetite. Considering the small polaron model, the electrical conductivity in the $Fe_{3-x}Cr_xO_4$ series was written as the probability that a given cationic site will contain an extra charge carrier, *i.e.*, that an electron from Fe^{2+}_{Oh} performs a successful hop to Fe^{3+}_{Oh}. Like bulk materials, the thin films depicted a general increase in the resistivity with higher x content, consistent with the decrease in the total number of conducting Fe^{2+}/Fe^{3+} pairs. Unlike bulk materials, smaller activation energies were found for higher Cr content films ($x = 1.2$). These differences were also related to the cationic site distribution. In fact, the films have greater inversion parameter and the favored Oh-to-Oh hopping pathway is still available for them, which results in smaller activation energy.

The cation distribution is therefore a key feature to consider for applications of $Fe_{3-x}Cr_xO_4$ thin films in future optoelectronic and spintronic devices as both band gap and exchange splitting in the conduction band can significantly change if the film assumes an inverse or normal spinel structure.

Acknowledgments

This project has been financially supported by CEA Saclay. XAS experiments were performed on the MARS and DEIMOS beamlines at SOLEIL Synchrotron, France (proposal number 99190116, 20191943). We are grateful to the SOLEIL staff for smoothly running the facility. The authors also

gratefully acknowledge financial support from the CNRS-CEA “METSA” French network (FR CNRS 3507), where the TEM micrographs were recorded.

References

[1] V.A.M. Brabers, Chapter 3 Progress in spinel ferrite research, in: Handbook of Magnetic Materials, Elsevier, 1995: pp. 189–324.
[2] I. Žutić, J. Fabian, S. Das Sarma, Spintronics: Fundamentals and applications, Reviews of Modern Physics. 76 (2004) 323–410.
[3] M. Bibes, A. Barthelemy, Oxide Spintronics, IEEE Transactions on Electron Devices. 54 (2007) 1003–1023.
[4] M. Alexe, M. Ziese, D. Hesse, P. Esquinazi, K. Yamauchi, T. Fukushima, S. Picozzi, U. Gösele, Ferroelectric Switching in Multiferroic Magnetite (Fe_3O_4) Thin Films, Advanced Materials. 21 (2009) 4452–4455.
[5] J.-B. Moussy, From epitaxial growth of ferrite thin films to spin-polarized tunnelling, Journal of Physics D: Applied Physics. 46 (2013) 143001.
[6] S. Matzen, P. Sainctavit, C. Gatel, B. Warot-Fonrose, Y. Zheng, Epitaxial growth and ferrimagnetic behavior of $MnFe_2O_4$(111) ultrathin layers for room-temperature spin filtering, Physical Review B. (2011) 10.
[7] J.J. Wisser, A.J. Grutter, D.A. Gilbert, A.T. N’Diaye, C. Klewe, P. Shafer, E. Arenholz, Y. Suzuki, S. Emori, Damping Enhancement in Coherent Ferrite–Insulating-Paramagnet Bilayers, Phys. Rev. Applied. 12 (2019) 054044. https://doi.org/10.1103/PhysRevApplied.12.054044.
[8] S. Emori, B.A. Gray, H.-M. Jeon, J. Peoples, M. Schmitt, K. Mahalingam, M. Hill, M.E. McConney, M.T. Gray, U.S. Alaan, A.C. Bornstein, P. Shafer, A.T. N’Diaye, E. Arenholz, G. Haugstad, K.-Y. Meng, F. Yang, D. Li, S. Mahat, D.G. Cahill, P. Dhagat, A. Jander, N.X. Sun, Y. Suzuki, B.M. Howe, Coexistence of Low Damping and Strong Magnetoelastic Coupling in Epitaxial Spinel Ferrite Thin Films, Advanced Materials. 29 (2017) 1701130. https://doi.org/10.1002/adma.201701130.
[9] L. Zhao, Z.-R. Lin, X. Ma, Y.-H. Dong, Catalytic activity of different iron oxides: Insight from pollutant degradation and hydroxyl radical formation in heterogeneous Fenton-like systems, Chemical Engineering Journal. 352 (2018) 343–351.
[10] F. Magalhães, M.C. Pereira, S.E.C. Botrel, J.D. Fabris, W.A. Macedo, R. Mendonça, R.M. Lago, L.C.A. Oliveira, Cr-containing magnetites $Fe_{3-x}Cr_xO_4$: The role of Cr^{3+} and Fe^{2+} on the stability and reactivity towards H_2O_2 reactions, Applied Catalysis A: General. 332 (2007) 115–123.
[11] G.C. Wood, High-temperature oxidation of alloys, Oxidation of Metals. 2 (1970) 47.
[12] I. Saeki, H. Konno, R. Furuichi, The initial oxidation of type 430 stainless steel in O2-H2O-N2 atmospheres at 1273 K, Corrosion Science. 38 (1996) 19–31.
[13] J. Ma, V.O. Garlea, A. Rondinone, A.A. Aczel, S. Calder, C. dela Cruz, R. Sinclair, W. Tian, S. Chi, A. Kiswandhi, J.S. Brooks, H.D. Zhou, M. Matsuda, Magnetic and structural phase transitions in the spinel compound $Fe_{1+x}Cr_{2-x}O_4$, Physical Review B. 89 (2014).
[14] A. Boudjemaa, R. Bouarab, S. Saadi, A. Bouguelia, M. Trari, Photoelectrochemical H_2-generation over Spinel $FeCr_2O_4$ in X^{-2} solutions ($X^{-2} = S^{-2}$ and SO_3^{-2}), Applied Energy. 86 (2009) 1080–1086.
[15] M. Robbins, G.K. Wertheim, R.C. Sherwood, D.N.E. Buchanan, Magnetic properties and site distributions in the system $FeCr_2O_4$-Fe_3O_4($Fe^{2+}Cr_{2-x}Fe_x^{3+}O_4$, Journal of Physics and Chemistry of Solids. 32 (1971) 717–729.
[16] H.N. Ok, L.S. Pan, B.J. Evans, Fe^{57} Mössbauer study of chromium-doped magnetite, $Fe_{3-x}Cr_xO_4$($0 \leq x \leq 0.5$) above the Verwey transition, Physical Review B. 17 (1978) 85–90.
[17] K. Kose, S. Iida, Interacting phase transitions in $Fe_{1+x}Cr_{2-x}O_4$ ($0 \leq x \leq 0.4$), Journal of Applied Physics. 55 (1984) 2321–2323.
[18] H.J. Levinstein, M. Robbins, C. Capio, B. Laboratories, M. Hill, A crystallographic study of the system $FeCr_2O_4$-Fe_3O_4 ($Fe^{2+}Fe^{3+}{}_xCr_{2-x}O_4$), Materials Research Bulletin. 7 (1972) 27–34.
[19] E.J. Verwey, P.W. Haayman, F.C. Romeijn, Physical Properties and Cation Arrangement of Oxides with Spinel Structures II. Electronic Conductivity, The Journal of Chemical Physics. 15 (1947) 181–187.
[20] S.A. Chambers, T.C. Droubay, T.C. Kaspar, I.H. Nayyar, M.E. McBriarty, S.M. Heald, D.J. Keavney, M.E. Bowden, P.V. Sushko, Electronic and Optical Properties of a Semiconducting Spinel (Fe_2CrO_4), Advanced Functional Materials. 27 (2017) 1605040.

[21] J. Nell, B. Wood, High temperature electrical measurements and thermodynamic properties of Fe3O4-FeCr2O4-MgCr2O4-FeAl2O4 spinels, American Mineralogist. 76 (1991) 405–426.
[22] D.S. Lee, G. Chern, Electrical transport properties of $Fe_{3-x}Cr_xO_4$ ferrite films on MgO (001) grown by molecular beam epitaxy, Physica B: Condensed Matter. 407 (2012) 297–301.
[23] C.-L. Chen, C.-L. Dong, K. Asokan, G. Chern, C.L. Chang, Electronic structure of Cr doped Fe_3O_4 thin films by X-ray absorption near-edge structure spectroscopy, Solid State Communications. 272 (2018) 48–52.
[24] J.A. Moyer, R. Gao, P. Schiffer, L.W. Martin, Epitaxial growth of highly-crystalline spinel ferrite thin films on perovskite substrates for all-oxide devices, Scientific Reports. 5 (2015).
[25] A.V. Ramos, J.-B. Moussy, M.-J. Guittet, A.M. Bataille, M. Gautier-Soyer, M. Viret, C. Gatel, P. Bayle-Guillemaud, E. Snoeck, Magnetotransport properties of Fe_3O_4 epitaxial thin films: Thickness effects driven by antiphase boundaries, Journal of Applied Physics. 100 (2006) 103902.
[26] X. Wang, Y. Liao, D. Zhang, T. Wen, Z. Zhong, A review of Fe_3O_4 thin films: Synthesis, modification and applications, Journal of Materials Science & Technology. 34 (2018) 1259–1272.
[27] C. Bataillon, F. Bouchon, C. Chainais-Hillairet, C. Desgranges, E. Hoarau, F. Martin, S. Perrin, M. Tupin, J. Talandier, Corrosion modelling of iron based alloy in nuclear waste repository, Electrochimica Acta. 55 (2010) 4451–4467.
[28] N. Jedrecy, T. Aghavnian, J.-B. Moussy, H. Magnan, D. Stanescu, X. Portier, M.-A. Arrio, C. Mocuta, A. Vlad, R. Belkhou, P. Ohresser, A. Barbier, Cross-Correlation between Strain, Ferroelectricity, and Ferromagnetism in Epitaxial Multiferroic CoFe2O4/BaTiO3 Heterostructures, ACS Appl. Mater. Interfaces. 10 (2018) 28003–28014. https://doi.org/10.1021/acsami.8b09499.
[29] B. Sitaud, P.L. Solari, S. Schlutig, I. Llorens, H. Hermange, Characterization of radioactive materials using the MARS beamline at the synchrotron SOLEIL, Journal of Nuclear Materials. 425 (2012) 238–243.
[30] I. LLorens, P.L. Solari, B. Sitaud, R. Bes, S. Cammelli, H. Hermange, G. Othmane, S. Safi, P. Moisy, S. Wahu, C. Bresson, M.L. Schlegel, D. Menut, J.-L. Bechade, P. Martin, J.-L. Hazemann, O. Proux, C. Den Auwer, X-ray absorption spectroscopy investigations on radioactive matter using MARS beamline at SOLEIL synchrotron, Radiochimica Acta. 102 (2014) 957–972.
[31] B. Ravel, M. Newville, ATHENA, ARTEMIS, HEPHAESTUS: data analysis for X-ray absorption spectroscopy using IFEFFIT., J Synchrotron Radiat. 12 (2005) 537–541.
[32] P. Ohresser, E. Otero, F. Choueikani, K. Chen, S. Stanescu, F. Deschamps, T. Moreno, F. Polack, B. Lagarde, J.-P. Daguerre, F. Marteau, F. Scheurer, L. Joly, J.-P. Kappler, B. Muller, O. Bunau, Ph. Sainctavit, DEIMOS: A beamline dedicated to dichroism measurements in the 350–2500 eV energy range, Review of Scientific Instruments. 85 (2014) 013106.
[33] L. Joly, E. Otero, F. Choueikani, F. Marteau, L. Chapuis, P. Ohresser, Fast continuous energy scan with dynamic coupling of the monochromator and undulator at the DEIMOS beamline, Journal of Synchrotron Radiation. 21 (2014) 502–506.
[34] M.W. Haverkort, G. Sangiovanni, P. Hansmann, A. Toschi, Y. Lu, S. Macke, Bands, resonances, edge singularities and excitons in core level spectroscopy investigated within the dynamical mean-field theory, Europhysics Letters. 108 (2014) 57004.
[35] M.W. Haverkort, M. Zwierzycki, O.K. Andersen, Multiplet ligand-field theory using Wannier orbitals, Physical Review B. 85 (2012).
[36] Y. Lu, M. Höppner, O. Gunnarsson, M. W. Haverkort, Efficient real frequency solver for dynamical mean field theory, Physical Review B. 90 (2014).
[37] M. Retegan, Crispy: version 0.7.3, 2019. https://dx.doi.org/10.5281/zenodo.1008184.
[38] É. Gaudry, P. Sainctavit, F. Juillot, F. Bondioli, P. Ohresser, I. Letard, From the green color of eskolaite to the red color of ruby: an X-ray absorption spectroscopy study, Phys Chem Minerals. 32 (2006) 710–720. https://doi.org/10.1007/s00269-005-0046-x.
[39] S. Brice-Profeta, Magnetic order in g-Fe2O3 nanoparticles: a XMCD study, Journal of Magnetism and Magnetic Materials. (2005) 12.
[40] H. Elnaggar, R. Wang, M. Ghiasi, M. Yañez, M.U. Delgado-Jaime, M.H. Hamed, A. Juhin, S.S. Dhesi, F. de Groot, Probing the local distortion of Fe sites in Fe_3O_4 thin films using enhanced symmetry selection in XMLD, Physical Review Materials. 4 (2020).
[41] R.F.L. Evans, W.J. Fan, P. Chureemart, T.A. Ostler, M.O.A. Ellis, R.W. Chantrell, Atomistic spin model simulations of magnetic nanomaterials, 26 (2014) 103202.

[42] J.-B. Moussy, S. Gota, A. Bataille, M.-J. Guittet, M. Gautier-Soyer, F. Delille, B. Dieny, F. Ott, T. Doan, P. Warin, P. Bayle-Guillemaud, C. Gatel, E. Snoeck, Thickness dependence of anomalous magnetic behavior in epitaxial Fe3O4(111) thin films: Effect of density of antiphase boundaries, Phys. Rev. B. 70 (2004) 174448. https://doi.org/10.1103/PhysRevB.70.174448.
[43] M.H. Francombe, Lattice changes in spinel-type iron chromites, Journal of Physics and Chemistry of Solids. 3 (1957) 37–43.
[44] A.P. Grosvenor, B.A. Kobe, M.C. Biesinger, N.S. McIntyre, Investigation of multiplet splitting of Fe 2p XPS spectra and bonding in iron compounds, Surface and Interface Analysis. 36 (2004) 1564–1574.
[45] M.D. Scafetta, T.C. Kaspar, M.E. Bowden, S.R. Spurgeon, B. Matthews, S.A. Chambers, Reversible Oxidation Quantified by Optical Properties in Epitaxial $Fe_2CrO_4^{+\delta}$ Films on (001) $MgAl_2O_4$, ACS Omega. 5 (2020) 3240–3249.
[46] H.J. Yearian, J.M. Kortright, R.H. Langenheim, Lattice Parameters of the $FeFe_{(2-x)}Cr_xO_4$ Spinel System, The Journal of Chemical Physics. 22 (1954) 1196–1198.
[47] Néel, M. Louis, Propriétés magnétiques des ferrites: ferrimagnétisme et antiferromagnétisme, Annales de Physique. 12 (1948) 137–198.
[48] S. Celotto, W. Eerenstein, T. Hibma, Characterization of anti-phase boundaries in epitaxial magnetite films, The European Physical Journal B - Condensed Matter. 36 (2003) 271–279. https://doi.org/10.1140/epjb/e2003-00344-7.
[49] D.T. Margulies, F.T. Parker, M.L. Rudee, F.E. Spada, J.N. Chapman, P.R. Aitchison, A.E. Berkowitz, Origin of the Anomalous Magnetic Behavior in Single Crystal Fe 3 O 4 Films, Phys. Rev. Lett. 79 (1997) 5162–5165. https://doi.org/10.1103/PhysRevLett.79.5162.
[50] A. Bhargava, R. Eppstein, J. Sun, M.A. Smeaton, H. Paik, L.F. Kourkoutis, D.G. Schlom, M. Caspary Toroker, R.D. Robinson, Breakdown of the Small-Polaron Hopping Model in Higher-Order Spinels, Adv. Mater. 32 (2020) 2004490. https://doi.org/10.1002/adma.202004490.
[51] B. Gillot, F. Jemmali, A. Rousset, Kinetics and mechanism of ferrous spinel oxidation studied by electrical conductivity and thermogravimetry, Journal of Materials Science. 21 (1986) 4436–4442.
[52] R. Dieckmann, C.A. Witt, T.O. Mason, Defects and Cation Diffusion in Magnetite (V): Electrical Conduction, Cation Distribution and Point Defects in Fe3-δO4, Berichte Der Bunsengesellschaft Für Physikalische Chemie. 87 (1983) 495–503. https://doi.org/10.1002/bbpc.19830870609.
[53] J.P. Wright, J.P. Attfield, P.G. Radaelli, Long Range Charge Ordering in Magnetite Below the Verwey Transition, Physical Review Letters. 87 (2001) 266401.
[54] R.R. Heikes, R.W. Ure, S.J. Angello, J.E. Bauerle, Thermoelectricity: Science and Engineering, Interscience Publishers, 1961. https://books.google.fr/books?id=77EStUe0NFYC.
[55] I.G. Austin, N.F. Mott, Polarons in crystalline and non-crystalline materials, Advances in Physics. 18 (1969) 41–102.
[56] J.M. Honig, Electrical properties of metal oxides which have “hopping” charge carriers, J. Chem. Educ. 43 (1966) 76. https://doi.org/10.1021/ed043p76.
[57] H.N. Ok, L.S. Pan, B.J. Evans, Fe^{57} Mössbauer study of chromium-doped magnetite, $Fe_{3-x}Cr_xO_4$ ($0 \leq x \leq 0.5$) above the Verwey transition, Physical Review B. 17 (1978) 85–90.
[58] T. Pohlmann, Cation- and lattice-site-selective magnetic depth profiles of ultrathin Fe_3O_4 films, Physical Review B. (2020) 6.
[59] P. Wasilewski, D. Virgo, G.C. Ulmer, F.C. Schwerer, Magnetochemical characterization of $Fe(Fe_xCr_{2-x})O_4$ spinels, Geochimica et Cosmochimica Acta. 39 (1975) 889–902.
[60] P.K. Baltzer, P.J. Wojtowicz, M. Robbins, E. Lopatin, Exchange Interactions in Ferromagnetic Chromium Chalcogenide Spinels, (n.d.) 11.
[61] M. Robbins, Magnetic properties of chromium chalcogenide spinels, Geochimica et Cosmochimica Acta. 39 (1975) 883–888.